Impact of tunnel alignment on local seismic lining actions

Ahmad Mubarak*[1], Jonathan Knappett[2] and Michael Brown[3]

***Corresponding Author 1:**

Name: Ahmad Mubarak, BSc MSc PhD

Affiliation: Research Associate of Civil Engineering, University of Dundee, UK and CMS Survey, CERN, Switzerland

(**ORCID:** 0009-0002-9596-4824),

Contact address: Nethergate, Dundee DD1 4HN, United Kingdom,

email address: amubarak003@dundee.ac.uk

Author 2:

Name: Jonathan Knappett, MA MEng PhD CEng MICE

Affiliation: Professor of Civil Engineering, University of Dundee, UK

(**ORCID:** 0000-0003-1936-881X)

Contact address: Nethergate, Dundee DD1 4HN, United Kingdom,

email address: j.a.knappett@dundee.ac.uk

Author 3:

Name: Michael John Brown, BEng (Hons) PhD GMICE

Affiliation: Professor of Geotechnical Engineering, University of Dundee, UK

(**ORCID**: 0000-0001-6770-4836)

Contact address: Nethergate, Dundee DD1 4HN, United Kingdom,

email address: m.j.z.brown@dundee.ac.uk

(a)

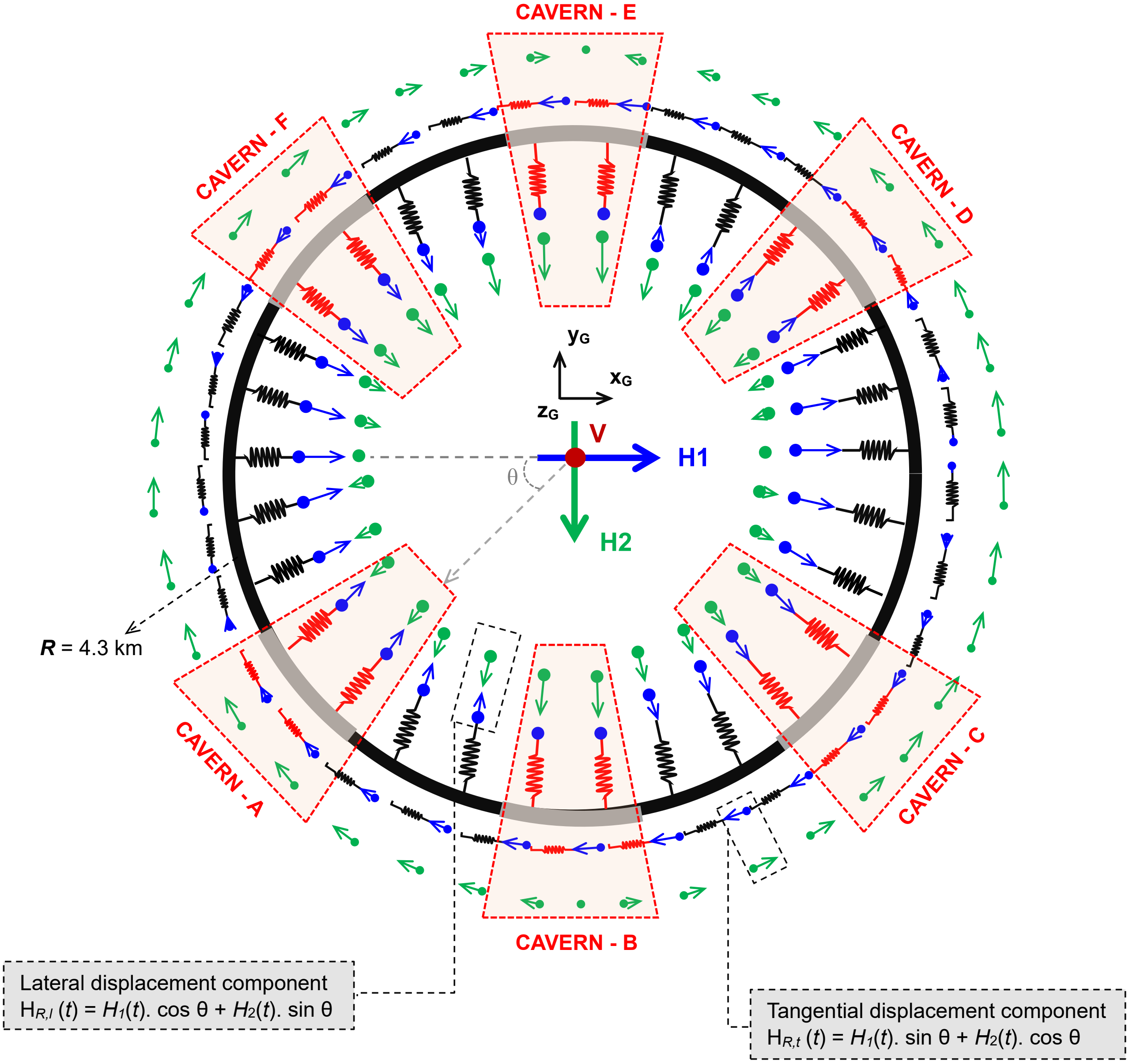

Lateral displacement component
$H_{R,l}\,(t) = H_1(t).\cos\theta + H_2(t).\sin\theta$

Tangential displacement component
$H_{R,t}\,(t) = H_1(t).\sin\theta + H_2(t).\cos\theta$

-

Abstract

The seismic performance of long, embedded tunnels can be significantly influenced by spatial variation in ground motion, particularly when the tunnel length approaches the wavelength of seismic waves. This study presents an integrated two-stage modelling approach to evaluate the effect of global (alignment-scale) effects on local (lining-scale) seismic response of the 27 km circular Large Hadron Collider (LHC) tunnel at CERN. A Beam-on-Nonlinear-Winkler-Foundation (BNWF) model is first used to simulate the effects of asynchronous wave-passage and alignment curvature under 3D seismic scenarios. The results reveal that asynchronous excitation induces wave-like differential displacements and non-planar forces, particularly intensified at tunnel-cavern interfaces due to stiffness contrasts. These global actions are then applied as dynamic boundary conditions in high-fidelity 3D nonlinear finite element analyses (FEA) of a critical tunnel section. The 3D FEA captures detailed local responses within the reinforced concrete lining, revealing that conventional 2D plane-strain models underestimate hoop forces and overlook alignment-induced amplifications of seismic actions. The results demonstrate the necessity of accounting for alignment effects in seismic tunnel design and demonstrate the effectiveness of the proposed BNWF–FEA hybrid methodology.

Key-words: Concrete Structures; Earthquakes; Finite Element Modelling; Numerical Modelling; Seismic Engineering; Tunnels

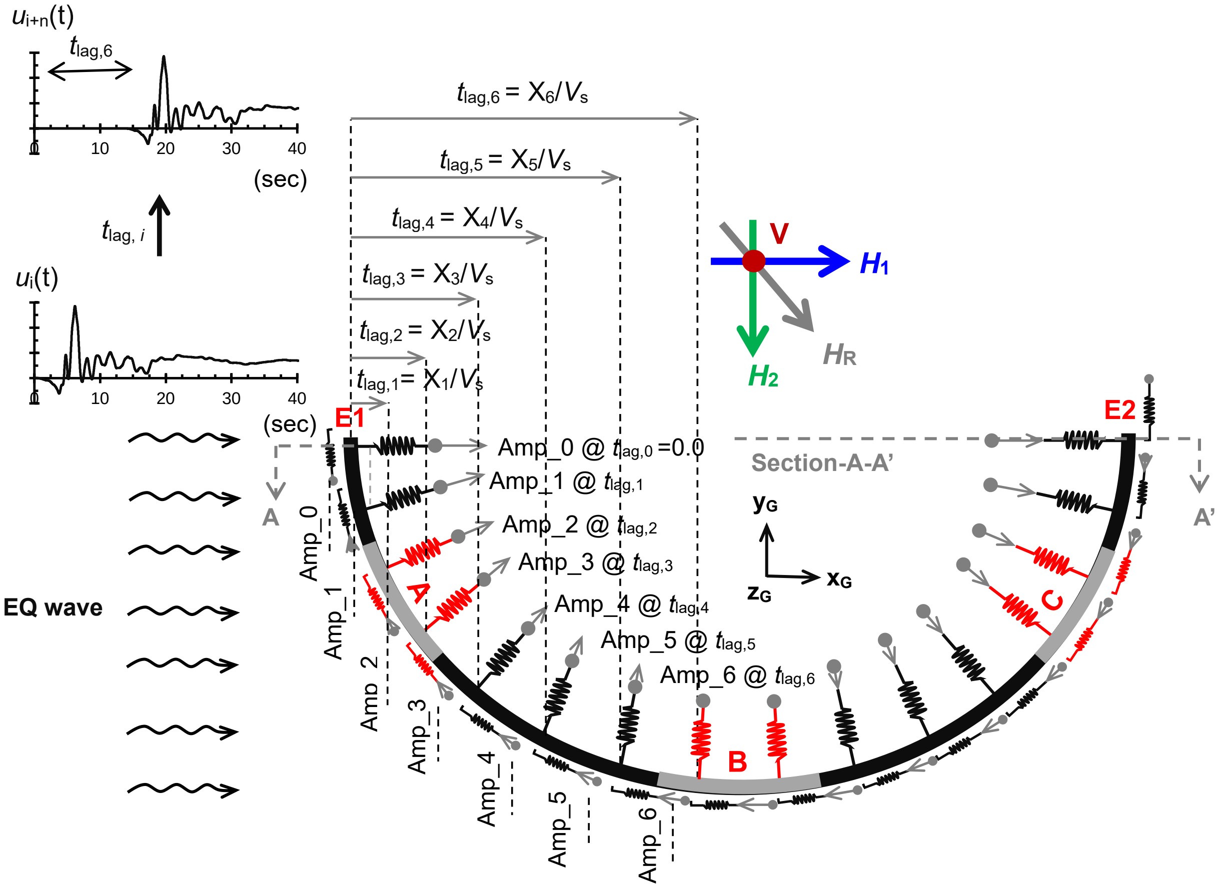

Figure 3 Assignment of the asynchronous amplitude vectors to the spring's boundaries

Impact of tunnel alignment on local seismic lining actions

Ahmad Mubarak*[1], Jonathan Knappett[2] and Michael Brown[3]

*Corresponding Author 1:

Name: Ahmad Mubarak, BSc MSc PhD

Affiliation: Research Associate of Civil Engineering, University of Dundee, UK and CMS Survey, CERN, Switzerland

(**ORCID:** 0009-0002-9596-4824),

Contact address: Nethergate, Dundee DD1 4HN, United Kingdom,

email address: amubarak003@dundee.ac.uk

Author 2:

Name: Jonathan Knappett, MA MEng PhD CEng MICE

Affiliation: Professor of Civil Engineering, University of Dundee, UK

(**ORCID:** 0000-0003-1936-881X)

Contact address: Nethergate, Dundee DD1 4HN, United Kingdom,

email address: j.a.knappett@dundee.ac.uk

Author 3:

Name: Michael John Brown, BEng (Hons) PhD GMICE

Affiliation: Professor of Geotechnical Engineering, University of Dundee, UK

(**ORCID**: 0000-0001-6770-4836)

Contact address: Nethergate, Dundee DD1 4HN, United Kingdom,

email address: m.j.z.brown@dundee.ac.uk

Date of revision: 3rd June. 2025

Number of words in the main text (excluding Abstract and References): 7005

Number of Figures: 15

Number of Tables: 0

***Corresponding author:**

Ahmad Mubarak
School of Science & Engineering
University of Dundee
DUNDEE
DD1 4HN
UK
Email: amubarak003@dundee.ac.uk

Abstract

The seismic performance of long, embedded tunnels can be significantly influenced by spatial variation in ground motion, particularly when the tunnel length approaches the wavelength of seismic waves. This study presents an integrated two-stage modelling approach to evaluate the effect of global (alignment-scale) effects on local (lining-scale) seismic response of the 27 km circular Large Hadron Collider (LHC) tunnel at CERN. A Beam-on-Nonlinear-Winkler-Foundation (BNWF) model is first used to simulate the effects of asynchronous wave-passage and alignment curvature under 3D seismic scenarios. The results reveal that asynchronous excitation induces wave-like differential displacements and non-planar forces, particularly intensified at tunnel-cavern interfaces due to stiffness contrasts. These global actions are then applied as dynamic boundary conditions in high-fidelity 3D nonlinear finite element analyses (FEA) of a critical tunnel section. The 3D FEA captures detailed local responses within the reinforced concrete lining, revealing that conventional 2D plane-strain models underestimate hoop forces and overlook alignment-induced amplifications of seismic actions. The results demonstrate the necessity of accounting for alignment effects in seismic tunnel design and demonstrate the effectiveness of the proposed BNWF–FEA hybrid methodology.

Key-words: Concrete Structures; Earthquakes; Finite Element Modelling; Numerical Modelling; Seismic Engineering; Tunnels

parallel dashpots were attached to the tunnel ring, shafts, and caverns with a tri-axial configuration at a spacing of l_s = 5m. The Winkler-type spring representation idealises the surrounding ground as a set of uncoupled springs and dashpots, which inherently neglects stress redistribution between adjacent tunnel segments. However, the tunnel is long between adjacent caverns in comparison to its diameter and is hence very slender. Under such circumstances it is reasonable to assume independence between adjacent tunnel segments. Mubarak *et al*. (2025) demonstrated that for a semi-circular alignment of similar size and mechanical properties and synchronous loading, the behaviour of the tunnel rapidly reduces to a plane strain response with distance away from the caverns. The nonlinear elastic stiffness and damping properties are reported in the supplementary material (stiffness – Fig A1 and Fig A2; damping – Fig A3) and were calibrated against a series of nonlinear 2D FE pseudo-static plane-strain analyses for the cavern, tunnel and shaft sections (the latter at different depths) conducted using PLAXIS 2D 2022. Further details of the calibration and validation procedures are outlined in Mubarak (2023) and Mubarak *et al*. 2025.

A full three-dimensional (3D) analysis was conducted, with the in-plane components (circumferential and radial) applied at each spring free boundary node having a trigonometric multiplier applied depending on the spring orientation with respect to the global axes. The in-plane resultant boundary amplitude vector 'H_R(t)' represents the vectorial sum of 'H_1(t)' and 'H_2(t)' local components resolved into components in directions circumferential and radial to the tunnel (i.e. in the direction of the springs) for each time step, as shown in Fig 2a. These components were assigned with a time shift along the tunnel alignment to mimic an asynchronous ground motion scenario, as discussed in the following section. The model does not explicitly simulate seismic wave reflections or refractions due to tunnel geometry or ground layering. Such effects can become significant for shallow tunnels at lower confining stresses $2z/D$ < 10 (where z is the running depth and D is the tunnel diameter; Yang *et al*., 2023), but the tunnels in this study are deep ($2z/D$ = 38).

The tunnel ring was meshed into 27,000 elements such that the length of individual elements was one-fifth the spacing between the adjacent springs. The general nonlinear dynamic analysis with implicit time integration scheme was selected for the analysis. To ensure convergence of the numerical solution, a quasi-static time stepping algorithm with a fixed increment size equal to the earthquake input motion time increment of 0.005 sec was employed. Newton's solution technique was selected to solve the set of nonlinear equilibrium equations and the displacement was set to vary linearly over each step. The model contains approximately 64,848 different features; Python scripts for generating different components are available online at DOI: 10.20933/100001310.

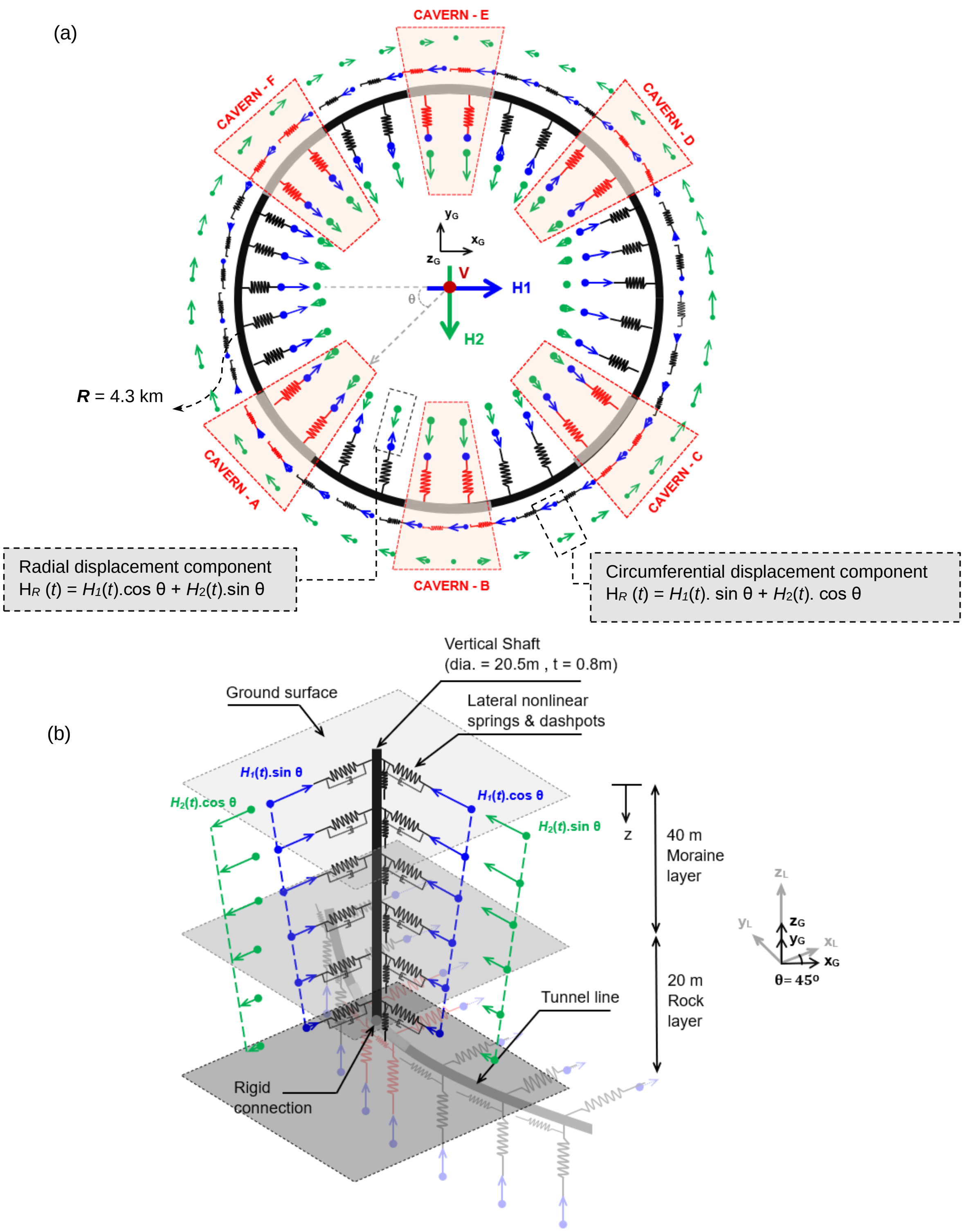

Fig 2 (a) Simplified sketch for the BNWF model of the circular LHC tunnel alignment and (b) vertical shafts; H_R (t): are the resultant dynamic displacement component in the radial and circumferential directions

3.1 *Asynchronicity*

Few explicit guidelines are proposed in the literature for estimating the lag-time of an asynchronous ground motion. Eurocode 8 (EN 1998- 1:2004) recommends a simple approach using the apparent shear wave velocity of the ground at the level of the tunnel (V_a) and the travel distance (X_i) in the direction of the travelling wave, as expressed in Eq.1.

$$t_{-lag,i} = X_i/V_a \qquad \text{Eq.1}$$

V_a is typically taken to be approximately equal to the shear wave velocity of the ground ($V_a \approx V_s \approx$ 1440 m/s, Fern *et al*. 2018) for underground structures embedded in deep rock rather than in shallow layers (Abrahamson *et al*. 1991; Power *et al*. 1996; Hashash *et al.* 2001).

Here, V_a was determined using available seismometer records for the selected earthquake motion from 10 seismic recording stations within the Geneva area. These stations were chosen at ground type-A locations (i.e. rock with $V_{s,30,} \geq 800$ m/s according to Eurocode 8). The arrival time (t_0) was then obtained from the available wave record at each station. Knowing the surficial distance, depth of the seismic source and the arrival time at each station, the apparent average shear wave velocity for the travelling wave was estimated within the rock formation as $V_{a,\,avg.} \approx$ 1140 m/s (supplementary material Table A1). To further simplify computation for the BNWF spring's amplitude vectors, $V_{a,\,avg.} \approx$ 1000 m/s was adopted. For this apparent velocity, the maximum total lag-time was estimated to be $t_{\text{lag, total}}$ = 8.6 sec across the whole LHC (i.e. from $E_1 \rightarrow E_2$ with alignment diameter of 8.6 km; Fig 3) assuming that: (i) the seismic waves pass through homogenous ground and thus reflections, refractions and wave incoherency can be ignored; and (ii) that the arrival time of the recorded motion at the rock outcrop was assumed approximately equal to the travel time in deep rock. Asynchronous excitation was applied following the Eurocode 8 methodology, applying free-field displacement time histories at each connector free node 'i' with a time lag determined using Eq.1, as shown schematically in Fig 3 for the bottom half of the circular alignment. The amplitudes were assigned from the left end 'E_1' towards the right end 'E_2' based on the assumption of an eastwards wave propagation.

The directionality of wave propagation was also investigated by assigning the amplitudes in three different directions to investigate the effect of directionality of wave propagation in relation to the locations of the caverns. These represented Eastwards propagation (from E_1 to E_2), North-eastwards (Cavern A to Cavern D) and Northwards (Cavern B to Cavern E). Due to the symmetry of the alignment and ground properties considered herein, these configurations represent the earthquake motion originating externally at 45-degree increments around the circumference of the LHC.

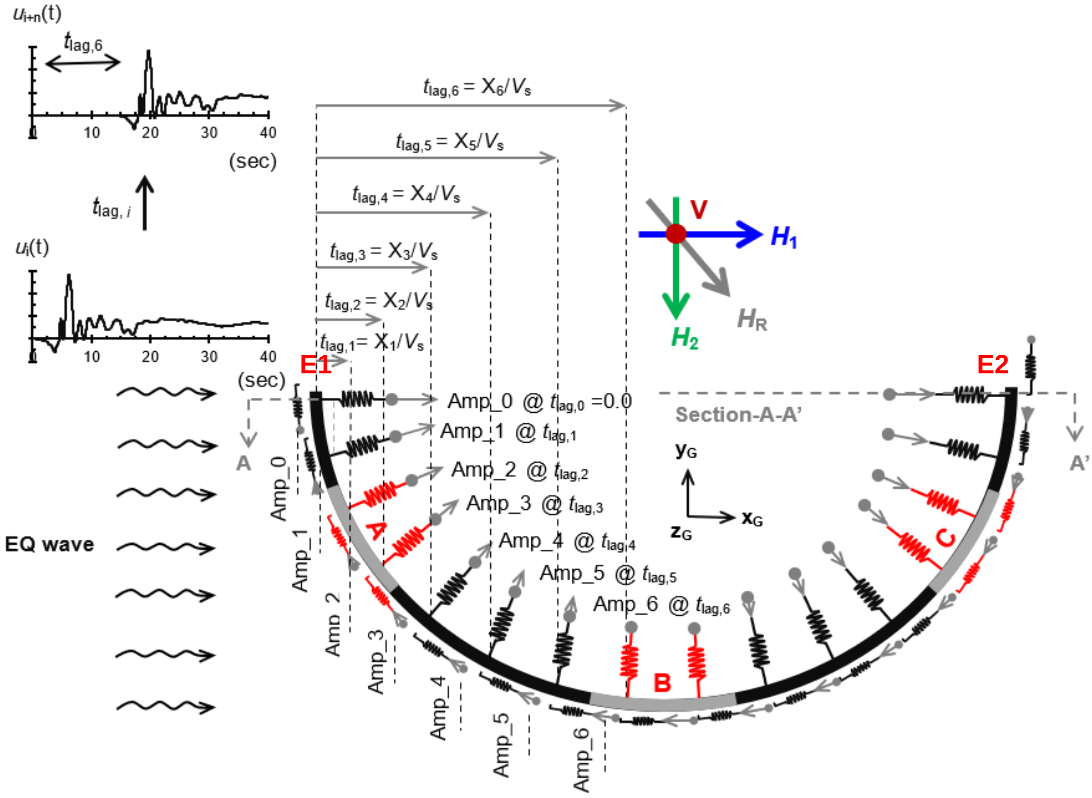

Fig 3 Assignment of the asynchronous amplitude vectors to the spring's boundaries showing Eastwards seismic wave propagation as an example

3.2 *Ground motion components*

A local outcrop earthquake was selected considering the local seismicity of the Geneva region, with a moment magnitude of $M_w = 4.5$, that was recorded by the Swiss National Seismological Service in 2005 at the Haute-Savoie province 55 km to the east of Geneva area. The acceleration time history was scaled consistently across all components such that $a_g = 0.15$ m/s^2 in the H_1 component according to the design peak ground acceleration (PGA) adopted for all CERN underground structures (supplementary material Fig A4). A low-pass filter was applied to limit the frequency content to $<$ 20Hz. The waveform is available at the Engineering Strong Motion (ESM) database by Luzi *et al*. (2016), ESM ID: IT-2005-0116.

Site-specific non-linear time history analyses were conducted separately using each of the individual earthquake components as an input motion in PLAXIS 2D (model details in Mubarak *et al.* 2023). Ground displacement amplitude time histories were then extracted from free-field points at spring/dashpots elevations for the tunnel and vertical shafts (supplementary material Fig. A5 and Fig. A6) and used as the input displacements at each spring free boundary node in the BNWF model.

4. 3-D Finite element analysis (FEA; local scale)

The 3-D FEA considered a short length of the tunnel close to the tunnel-cavern A connection which was identified to be the most heavily loaded at the alignment scale from the BNWF model. Two cases were considered, representing different tunnel-end boundary conditions, representing actions from synchronously- and asynchronously-excited global BNWF models. Due to the small size of the time-steps required during calculation and the deep running depth of the tunnel, the model was truncated vertically (Fig 4). The tunnel centreline is at a depth of 92 m below the ground surface and the confining stress from the ground above the modelled domain was incorporated as a constant applied vertical total stress of σ_z = 1916 kPa to ensure that the stress states and corresponding constitutive behaviour in the tunnel lining and surrounding rock were captured appropriately. The circular tunnel had a diameter of D = 5.2 m and the model domain had a depth z = 38m ($\approx 7D$) with rock cover of approximately 10m above the tunnel (where a much weaker rock layer was located) and a length y = 30 m (= $L_{crit.}$ at Cavern A). The width of the model x = 50 m ($\approx 10D$) was selected based on the results of previous plane-strain (2D) dynamic analyses for the tunnel section (Mubarak et al., 2024) such that the induced stresses around the structure degraded to the free-field conditions prior to the boundaries. The model domain was discretised into 32,273 10-noded tetrahedral elements (52,213 nodes). The mesh in the ground around the tunnel in the middle portion was refined into elements with characteristic length 'l_e' less than approximately one-tenth to one-eighth of the minimum wavelength (λ_{min}) associated with the maximum frequency (f_{max}) of the input motion (Bathe, 2006).

The analyses were each conducted in eight phases. The first seven phases modelled the initial conditions (deformations and stresses) associated with sequential excavation of the tunnel in the axial direction (+y-axis; Fig 4a), where soil volumes were progressively deactivated to provide stress relief, assuming full face excavation progresses in sections of 5 m followed by activating the RC tunnel lining at the end of each 5 m excavation stage. This approach assumed ideal conditions with no volume loss, which was considered reasonable as the tunnel is completely embedded within competent rock and was constructed using a Tunnel Boring Machine (TBM) with earth pressure balancing (Laughton, 1989). Earthquake ground motion was applied in the final (dynamic) phase, in which prescribed displacement time-histories were applied in three orthogonal directions at the bottom surface of the model based on those applied to the global BNWF model at the tunnel-cavern connection (i.e. considering the location of the modelled tunnel section with respect to the alignment geometry and direction of the applied seismic motion in relation to the alignment) and with free-field (tied node) side boundaries.

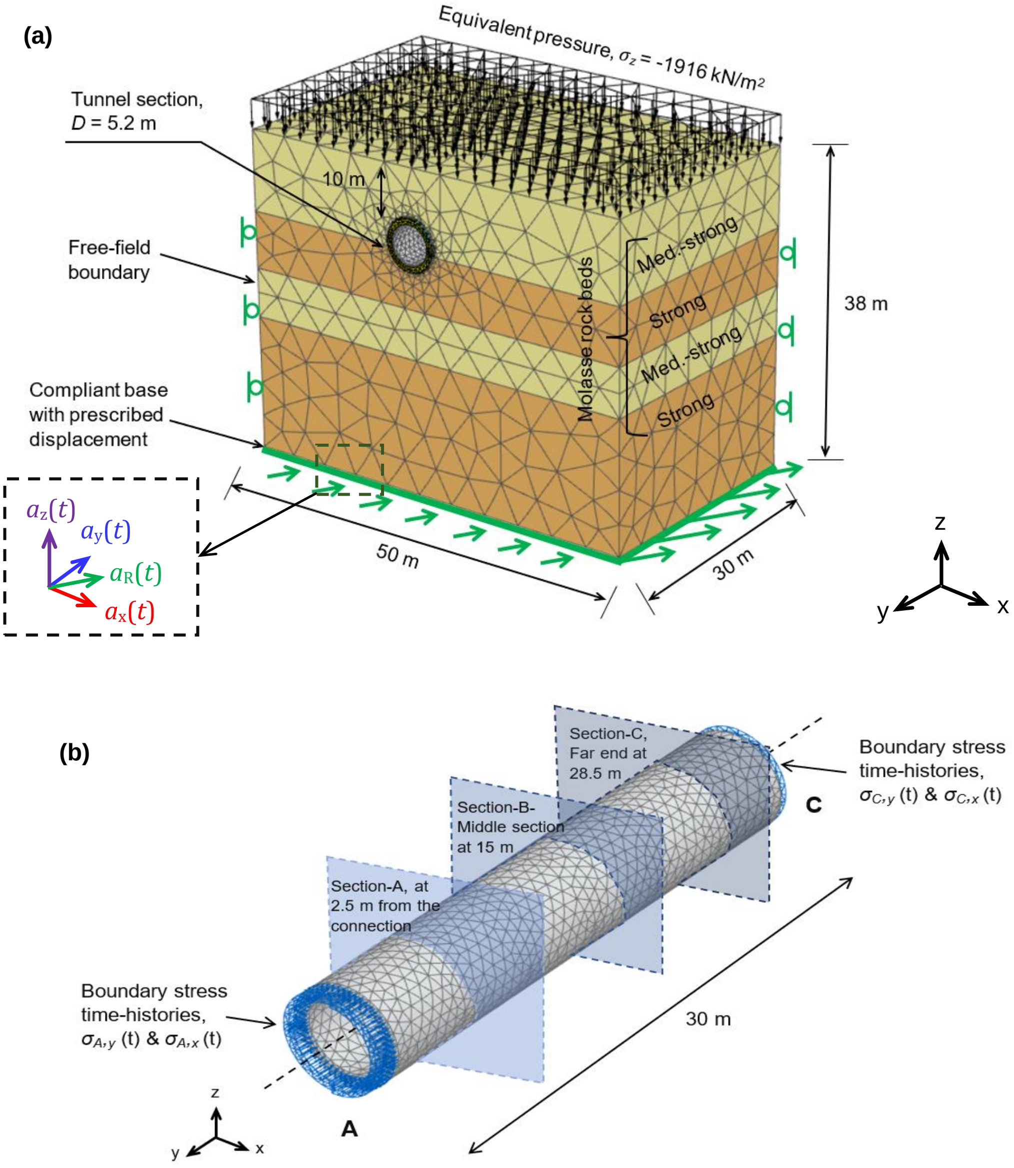

Fig 4 (a) 3D FE model domain of the longitudinal section at the critical region near the tunnel-cavern-A connection, and (b) FE model of the modelled 3D longitudinal tunnel lining only, showing the location of key tunnel cross sections for result extraction.

For seismic analysis, free-field and compliant base boundary conditions were used at the truncated lateral and bottom boundaries respectively, as proposed by Zienkiewicz *et al.* (1989), with normal and tangential relaxation coefficients $C_1 = 1$ and C_2=0.25, respectively. The Newmark numerical scheme was used for solving the equations of motion (Katona and Zienkiewicz, 1985), with time integration parameters $\alpha_N = 0.25$ and $\beta_N = 0.5$ which ensured the stability of the numerical solution by adding numerical damping to dissipate spurious higher-frequency oscillations (e.g., Kontoe *et al.* 2008).

4.1 *Longitudinal tunnel section*

Volume elements were used to model the concrete lining with embedded elasto-plastic plates for the reinforcing mesh, consistent with the approach described by and validated by Mubarak *et al.* (2023, 2024). The concrete has a compressive strength of 28 MPa (Grade C25/30 according to EN 1992-1-1: 2004) and was modelled using the nonlinear Concrete Model (Schweiger *et al.* 2014) available in the PLAXIS materials library with input parameters summarised in supplementary material Table B1. This modelling approach for RC was previously validated against experimental tests from the literature in Mubarak *et al*. (2023, 2024). Table B2 summarises the equivalent flexural (*EI*) and axial (*EA*) stiffnesses of the plate element used to model the longitudinal mesh reinforcement above and below the neutral axis assuming an elasto-plastic behaviour. The model, as calibrated, implicitly accounts for material damping in the range of 7%–10% (Mubarak *et al.* 2024), consistent with values for reinforced concrete recommended by Newmark and Hall (1982). Section reinforcement had 6T22/m top and bottom bars (area of steel, $A_s = 2281 \text{mm}^2/\text{m}$) with modulus of elasticity E_s=210 GPa, a tensile yield stress of f_y=460 MPa (class B500 according to BS 4449:2005) and tensile capacity $N_p = f_{ys}.A_s$. A dummy plate element was embedded at the middle of the tunnel section to extract the hoop forces which had elasto-plastic behaviour with a reduced flexural (*EI*) and axial (*EA*) stiffnesses equal to the stiffness of the reinforced hoop scaled by ($\times 10^{-6}$), such that it did not influence the structural stiffness of the RC lining.

Fig 5 shows the tunnel cross section (N-M) capacity interaction diagram and the moment-curvature (M-κ) diagram obtained from PLAXIS and also the nonlinear sectional analysis program Response-2000 (Bentz and Collins 2000). The moment-curvature behaviour shown in Fig 5b was consistent with the *EI* incorporated within the BNWF model.

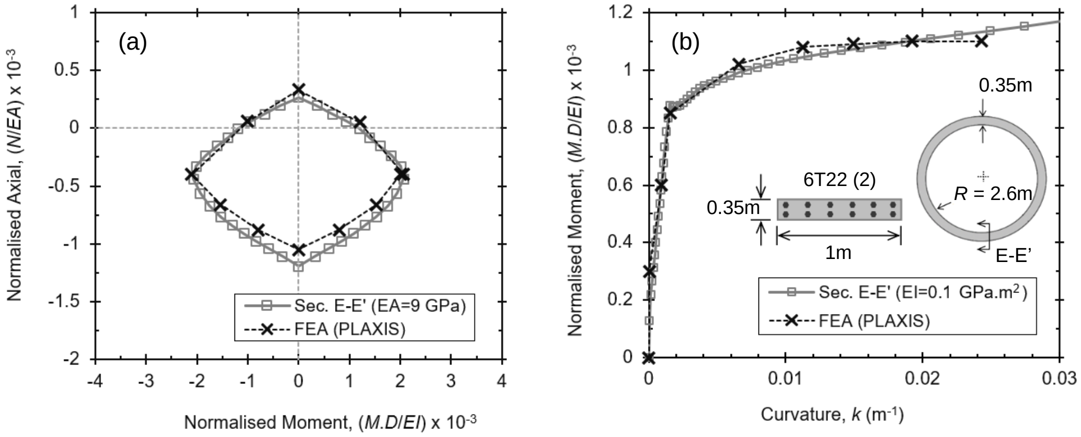

Fig 5 (a) Normalised Axial-Normalised Moment (N-M) interaction diagram, and (b) Normalised Moment-Curvature (M-κ) of the LHC tunnel section

4.2 *Ground profile and constitutive modelling*

The ground profile consisted of a complex and alternating sequence of horizontally bedded layers of Molasse rock with varying thicknesses, strength, and material properties (GADZ, 1996). Two types of rock units were identified at the running (centreline) depth of the tunnel with 'medium' to 'strong' rock strength and stiffness properties determined based on statistical analysis of a wide range of field data (e.g., GADZ 1996 a & b, GADZ 1998, Madinier *et al. 2017,* Fern *et al.* 2018). The constitutive behaviour was identical to that used in the 2D plane strain analyses used to calibrated the BNWF spring/dashpot properties (Mubarak *et al*. 2025). The Hardening Soil model with small strain stiffness (HS-small; Benz *et al.* 2009) was used with equivalent strength properties calibrated against the available Hoek-Brown failure envelopes of each rock unit over a stress range 0-6 MPa (Mubarak *et al*. 2024). Table B3 (supplementary material) summaries the constitutive parameters for each rock unit (see Fig 4 for layering), where reference stiffness parameters were defined at a reference atmospheric pressure of p'_{ref} = 100 kPa. Inherent large-strain-dependent damping was present within the HS-small model. To account for ground damping at very small strains, Rayleigh (frequency-dependent) damping was set to a target damping of D^*=1%, following the procedure defined by Amorosi *et al*. (2010), resulting in α_R = 0.13 and β_R = 0.00075 for target frequencies f_m=1.8 Hz and f_n = 2.46 Hz, based on a nonlinear 1D site response analysis in PLAXIS considering the local ground motion characteristics (Mubarak *et al*. 2024).

4.3 *Boundary conditions*

Due to the reduced size of the 3-D model, with the bottom boundary at approximately 23 m below the tunnel level, the input base motions in the ground were obtained from separate 1D FE non-linear site response analyses of the complete ground column in PLAXIS using the same constitutive modelling approach as described above (total depth of 200m, and nearly 120m of material below the tunnel level) with the input motion shifted in the time domain to represent the time at which the motion reaches the modelled section of the alignment (as considered for the BNWF model). The input motions at the bottom boundary of the 3-D FEA were extracted from the free-field profile at a level of approximately 109 m below ground level (BGL) equivalent to the bottom of the 3D FEA model. The components in the xy-plane had a directionality multiplier of 0.7 (= cos45° = sin45°), such that the resultant motion with respect to the global x-axis was consistent with the location of the modelled segment with respect to the direction of the applied ground motions (see Fig 6a, at Cavern A). The compliant base implemented the prescribed displacement as an input dynamic load along with a viscous boundary. The lateral soil boundaries combined non-reflecting viscous boundaries and the appropriate free-field dynamic displacements (i.e. simulating tied nodes laterally) but did not capture dynamic variation in horizontal stress due to wave-passage effects within the ground (e.g. due to surface waves). While this provides a practical approximation, its limitations—particularly under asynchronous excitation—should be recognised.

On the tunnel boundaries (A and C, where end 'A' is at the tunnel-cavern A connection point and the far end 'C' is in the tunnel at L_{crit} =30m from the cavern; Fig 4b) the resultant global tunnel actions obtained from the BNWF model for both synchronous and asynchronous cases at the alignment scale were imposed as equivalent dynamic stresses (Fig 6 a and b). Six-component action time-histories at homologous points near cavern-A were extracted from the BNWF models, namely; Axial force '$N_x(t)$', Moments '$M_z(t)$ & $M_y(t)$', Shear forces '$V_y(t)$ & '$V_z(t)$' and Torque '$T(t)$' (Fig 6b). The action time-histories are shown in supplementary material Fig B1 and Fig B2 for synchronous and asynchronous ground motion conditions, respectively.

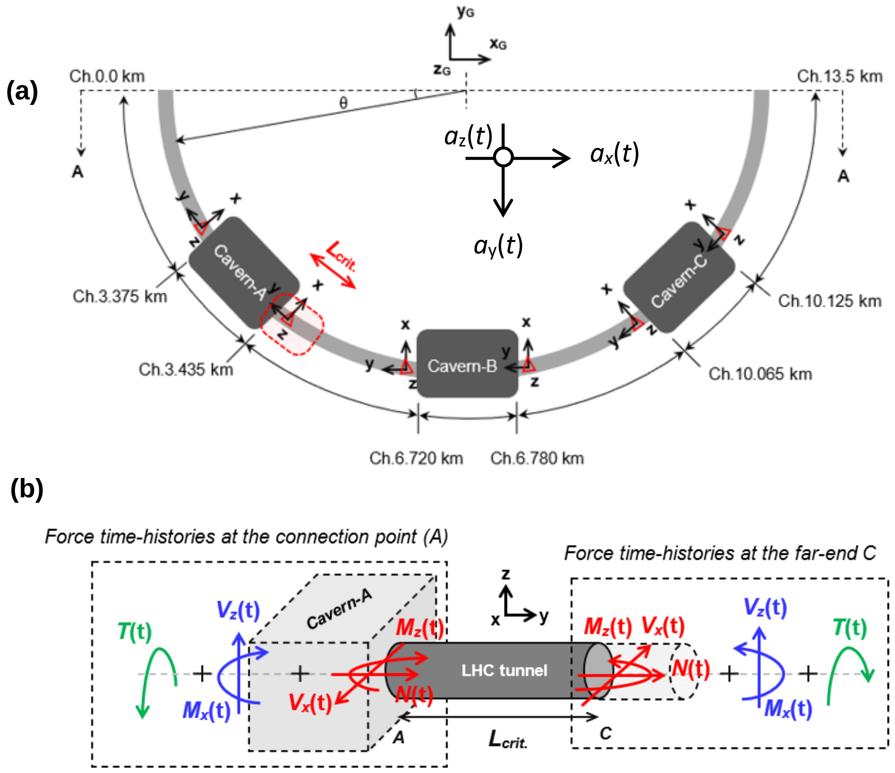

Fig 6 (a) Schematic view of the location of the modelled longitudinal tunnel segment and (b) the different action components in the 'in-plane' and 'out-of-plane' directions that were obtained from the BNWF model of the circular LHC tunnel at the critical region near Cavern-A.

The actions out of the horizontal plane of the tunnel alignment ($V_z(t)$, $M_x(t)$ and $T(t)$) in Fig B1 (d-f) and Fig B2 (d-f)) had very small amplitudes compared to the actions in the plane of the alignment ($N_y(t)$, $M_z(t)$ and $V_x(t)$) in Fig B1 (a-c) and Fig B2 (a-c). The ratios of out-of-plane to in-plane actions of the peak synchronous forces were $M_x/M_z \approx 0.03\%$, $V_z/V_x \approx 0.2\%$ and $T/M_z < 0.0001\%$, and for the asynchronous forces were $M_x/M_z \approx 1\%$, $V_z/V_x \approx 3\%$ and $T/M_z < 0.003\%$. This demonstrates that despite the 3-D excitation of the 3-D global alignment, the global actions out of the horizontal plane of the tunnel alignment were negligibly small and were hence neglected.

The dynamic stresses applied to the tunnel faces are illustrated schematically in supplementary material Fig B3. The axial (N) and shear forces (V_x) were converted to uniform stress distributions by dividing the force time-histories by the hoop cross sectional area (A_{hoop} = 5.33 m^2). These were applied normal to and in the plane of the tunnel cross-section, respectively. The in-plane moment (M_z) was modelled as equivalent uniform stresses with equal positive and negative values on the left and right side of the section (Fig B3a). The stresses were obtained by converting the moment time-history into a couple by dividing by the lever arm (≈2.2 m) between centroids of each half of the tunnel and dividing by half the hoop area (0.5A$_{\mathrm{hoop}}$ = 2.66 m^2; Fig B3c). A similar approach could be applied to the out-of-plane moment and shear actions if they had not been negligibly small. The resultant axial and planar stress components were obtained by algebraic summation of the individual components in each quarter of the cross-section (Fig B3c).

The resultant stress time-histories considering synchronous and asynchronous motion components at each end of the 3-D FE tunnel segment are shown in Fig B4. The time of application of the asynchronous components (Fig B4 c & d) had only a very small differential time-lag (Δt-lag = 0.03 sec) between ends ‘A’ and ‘C’ due to the length of the modelled segment. Hence, ground motions were simultaneously applied to the lower rock surface of the 3D model in both synchronous and asynchronous cases. It should be noted that the combined (normal) boundary stress components are well below the compressive and tensile strength of the concrete (Table B1).

5. Results

5.1 *Effect of asynchronous wave propagation*

Fig 7 shows the envelope of peak seismic actions due to the asynchronous ground motion in the Eastwards direction from the asynchronous BNWF analysis along with a synchronous comparator. It can be seen in Fig 7b, e & h that the seismic demand at the alignment level is amplified significantly in the region of the tunnel-cavern connection (of length $L_{crit.} \approx 30$m from the cavern) under all shaking scenarios but is also increased along the entire tunnel length in the 3D asynchronous case (Fig 7a, d & g).

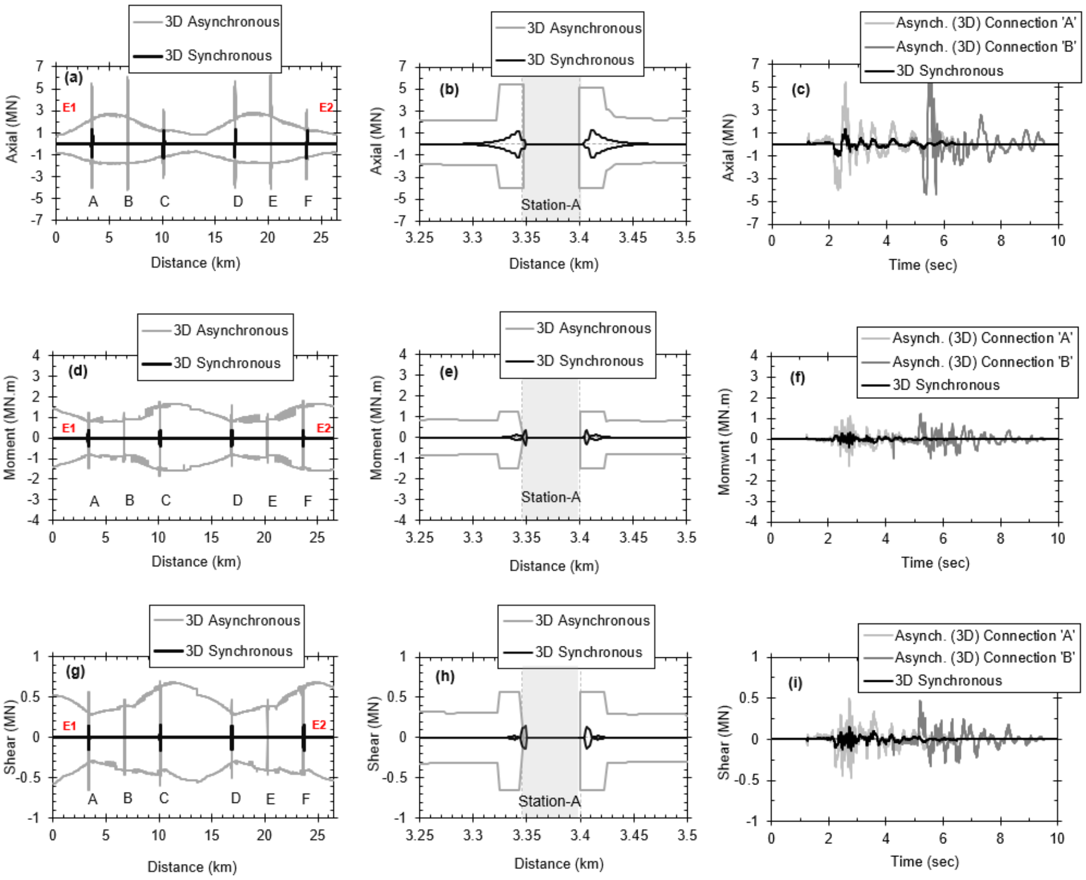

Fig 7 Peak seismic force envelopes due to 3-D Synchronous and Asynchronous Eastwards wave propagation, where (a), (d) & (g) are force distributions along the circular alignment; (b), (e) & (h) show forces at the tunnel-cavern-A connection; (c), (f) & (i) are time histories obtained at the connections to caverns 'A' &'B' respectively.

In both cases this effect is strongly linked to differential displacements due to the stiffness contrast between the cavern and tunnel (Mubarak *et al*. 2025), hence why it is seen even under synchronous conditions. In the asynchronous cases, bending deformations travelling along the alignment due to the passage of seismic waves amplify differential displacements and strengthen seismic demand at the tunnel-cavern connection. Neither effect can be observed in conventional 2-D plane-strain analyses of specific tunnel cross-sections and can only be observed at the alignment scale that is facilitated by the BNWF model presented herein.

5.2 *Effect of directionality of wave propagation*

Fig 8 shows the effect of the wave propagation direction on the resultant force envelopes along the tunnel alignment and at the tunnel-cavern connections. The force envelopes are effectively translated along the longitudinal axis, such that the tunnel-cavern connection points are less affected by the global actions when the propagation direction is transverse/perpendicular to the cavern axis. The consequence of this is that a different cavern-tunnel connection point will be most critical as the propagation direction changes, but the magnitude of the actions at the critical point will be similar if the motion characteristics of the propagating wave are the similar (e.g. Cavern B has the lowest global moment and shear actions for NE propagation, while Cavern C has the lowest global moment and shear for N propagation). In the case that the ground motion characteristics were significantly different depending on where they originated from (and hence the direction in which they propagate) the modelling approach presented herein would facilitate the rapid estimation of seismic actions from different earthquake scenarios identified from a probabilistic seismic hazard analysis.

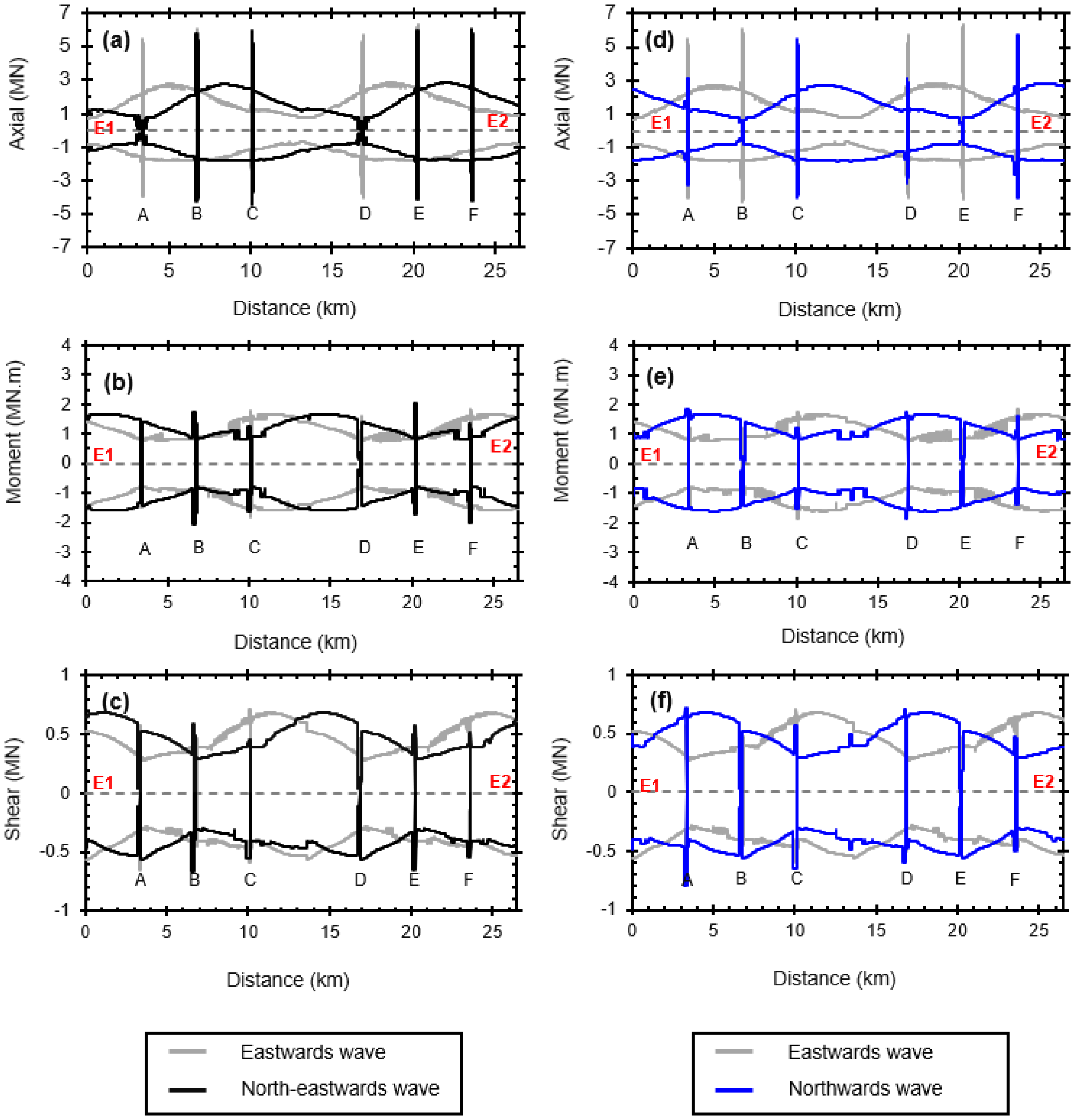

Fig 8 Directionality effect of propagated seismic wave on the peak seismic force envelopes along the circular alignment, where (a), (b) & (c) are force distributions due to North-eastwards propagation; (d), (e) & (f) are force distributions due to Northwards propagation, both compared with the Eastwards propagation.

5.3 *Maximum length of a synchronous tunnel model*

While many researchers have highlighted the importance of considering asynchronicity on the global response of long structures (e.g. Kramer 1996; Hashash *et al.* 2001), the literature lacks explicit guidelines for defining the limiting length beyond which asynchronous effects should be considered. It is here assumed that that for a seismic wave with a travelling velocity V_a (= V_s) with a range of low frequencies with sufficient strain energy to induce significant transverse deformations, the seismic wave will produce wave-like deformations (i.e. local bending in the tunnel alignment) if the tunnel is longer than the wavelength (λ).

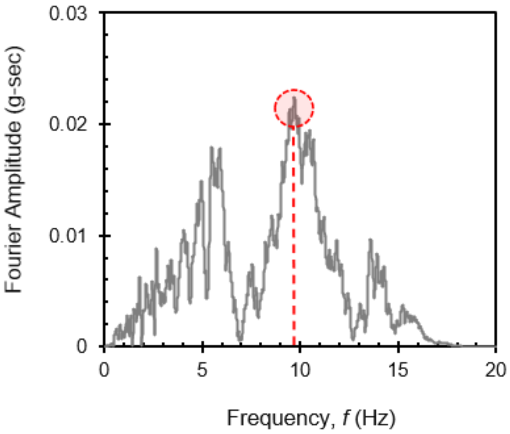

Fig 9 Fourier amplitude spectrum for dominant component of the local Swiss motion ($a_{H1}(t)$ with PGA = 0.15g)

In the case of the LHC, Fig 9 shows the Fourier spectrum of the motion used ($a_{H1}(t)$). The maximum Fourier amplitude corresponds to $f \approx 10$ Hz and there is no input energy beyond $f = 20$ Hz. Hence, for V_a = 1000 m/s, λ = 50-100 m. This suggests that the largest size of a 3-D section of a tunnel system that can be modelled in continuum FEA with a synchronous/uniform input ground motion is of the order of 100 m (in this case). For shallower tunnels running in ground with lower V_s the maximum length would be considerably shorter. Fig 7 (b, e, h) demonstrated that a critical region of the tunnel where subsequent continuum FEA would be required was the zone within approximately 30 m of the tunnel-cavern connection. These findings justify the use of the 30 m domain length in the 3-D continuum FEA and the use of a synchronous input motion across the base of the model for this section, so long as the dynamic boundary conditions at either end of this section (e.g. Fig 7 c, f, i) are included to capture the alignment scale asynchronicity effects.

5.4 *Effect of apparent wave velocity on the predicted alignment forces*

The accuracy of the estimated seismic wave travelling velocity over a wide area which extends to several square kilometres might incur a high level of uncertainty, given the numerous factors that affect wave transmission and coherency. The LHC tunnel (circumference of 27 km) passes through rock with varying properties and geological conditions with 1000 m/s < V_s < 1500 m/s (GADZ, 1998; GADZ, 1996). A parametric study was performed on the circular LHC alignment using the BNWF model considering asynchronous boundary amplitude vectors derived for $V_a = V_s$ = 800, 1000, 1500, 2000 and 2500 m/s. The lowest value represents the lower limit specified by Eurocode 8 for ground type-A (rock), while the upper limit of 2500 m/s was set to represent a much more competent rock. True synchronous effects are only expected if ground had a very high V_s (for the diameter of the LHC and smallest time step of the input motion, this would be $V_a = 1.72 \times 10^6$ m/s).

Fig 10 shows the variation of the tunnel alignment forces at three key locations with V_s, namely the tunnel-cavern ‘A’ & ’B’ connections and at a point along the tunnel line (CH. 5 km) midway between these caverns. In general, the induced alignment-scale seismic actions tend to decrease with increased V_a and appear to stabilise beyond V_a = 2500 m/s at the tunnel-cavern ‘A’ & ’B’ connections. This is consistent with stiffer rock reducing the difference in relative ground-structure interaction stiffness between the comparatively more flexible tunnel and the cavern. The transverse bending actions (moment and shear) were relatively unaffected by V_a far from the caverns (e.g. at CH. 5 km).

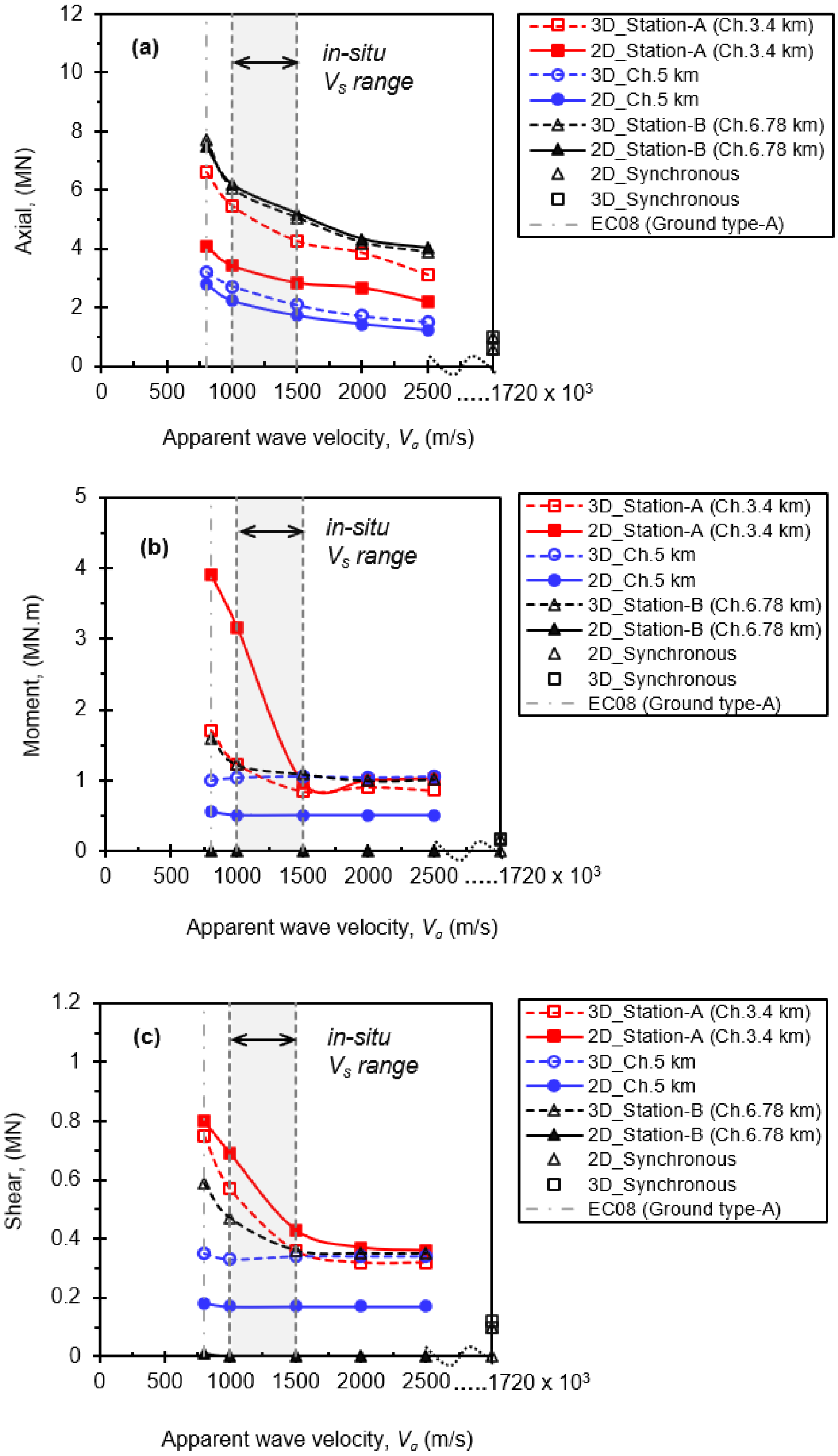

Fig 10 Effect of shear wave velocity (or wave travel time) on the tunnel alignment forces considering 2D and 3D wave combinations.

The decrease in alignment forces is also attributed to the range of wave lengths from the applied asynchronous motion being much wider with higher V_a. Given the slenderness of the tunnel section, slower wave velocities lead to shorter sections being subjected to local bending with sharper differential displacements, which are exacerbated at the tunnel-cavern connections. The in-situ range of V_s in the rock for the LHC site suggests that the modelling assumption of using a lower bound wave velocity (V_a =1000m/s) is conservative as it yields the maximum seismic forces within the range of V_s values considered.

5.5 *Local lining actions*

The time histories from the BNWF analyses in Fig 7 c, f & i were used as equivalent boundary stresses in the detailed local 3-D dynamic FEA of the critical tunnel sections, to assess the local section structural capacity against the induced asynchronous effects at the alignment scale. The 3-D FEA models were executed using a workstation having 6 Cores with 12 logical processors (Intel Xeon CPU @3.60GHz, 3601 Mhz) and a physical memory (RAM) = 32 GB. The run time to process the 5.5 seconds of the ground motion for the 30 m critical length considered was approximately 570,325 seconds (≈ 5.6 days). Although this could be significantly reduced using high performance computing capabilities, this demonstrates the difficulty there would be in modelling the complete 27 km global alignment using 3D continuum FEA, and also the value of the combined BNWF + limited 3D FEA approach proposed herein to enable analyses to be conducted on routinely available computing facilities and to also enable design changes to the alignment (global scale) or structural detailing (local scale) to be implemented within a practical timeframe.

Fig 11 shows the sign convention adopted in this section and Fig 4b indicates key transverse cross sections (A, B & C) where seismic actions in the RC lining are explored. The in-plane responses (hoop force N_1, lining moment M_{11} and lining shear Q_{13}) were compared with (conventional) 2-D plane strain FE dynamic analyses of the tunnel section utilising the same constitutive models and model parameters for the lining and surrounding ground (reported in

Mubarak *et al*. 2024). All responses were obtained at the time step at which the tunnel lining had maximum ovalisation, defined as the largest ratio of major to minor axis diameters of the deformed lining (see next section).

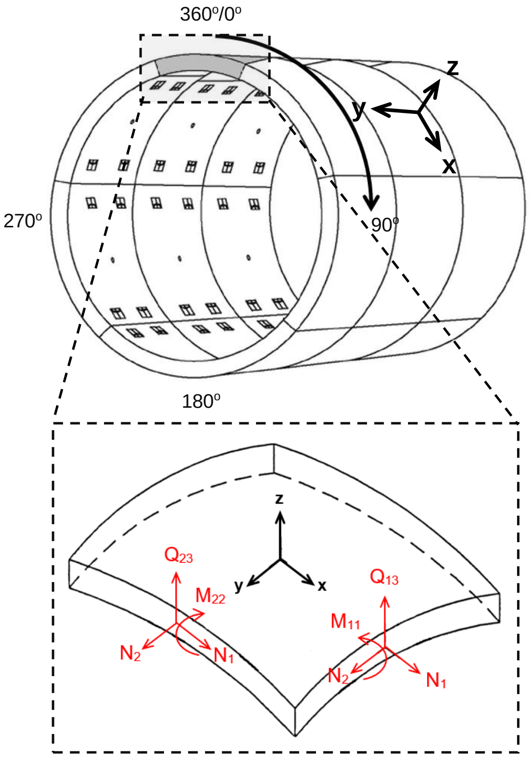

Fig 11 Sign convention for the obtained lining forces in the transverse (+*ve* x-axis) and the longitudinal/axial (+*ve* y-axis) directions. Note that (-*ve*) is compression.

Fig 12 shows the tunnel lining peak forces from transverse sections-A, B & C considering synchronous and asynchronous boundary conditions. The in-plane forces (Fig 12 a-c) were compared with 2-D plane strain analysis. The hoop forces (N_1) at each section were significantly smaller in compressive magnitude considering the synchronous alignment effects in 3-D than the predicted 2-D lining forces meaning that the bending moment capacity was lower in 3-D (Fig 5a). Simultaneously, the induced moments (M_{11} and shear forces Q_{13}) were increased in 3-D, such that the utilisation of the section was increased, though the magnitude of the actions was small for synchronous conditions.

The induced lining forces were significantly higher in the asynchronous case which are consistent with the larger magnitude of the alignment-level actions from the BNWF model. This impact cannot be predicted using the conventional 2-D or even 3-D analyses of a critical length of tunnel without considering the influence of asynchronicity from the alignment scale on the local tunnel response. For the asynchronous case, lining forces in the out-of-plane direction in (Fig 12 d-f) were significantly higher than those in-plane (Fig 12 a-c). In general, the largest actions around the circumference in all degrees of freedom were larger at section A which was closest to the tunnel-cavern connection where the stiffness contrast was highest.

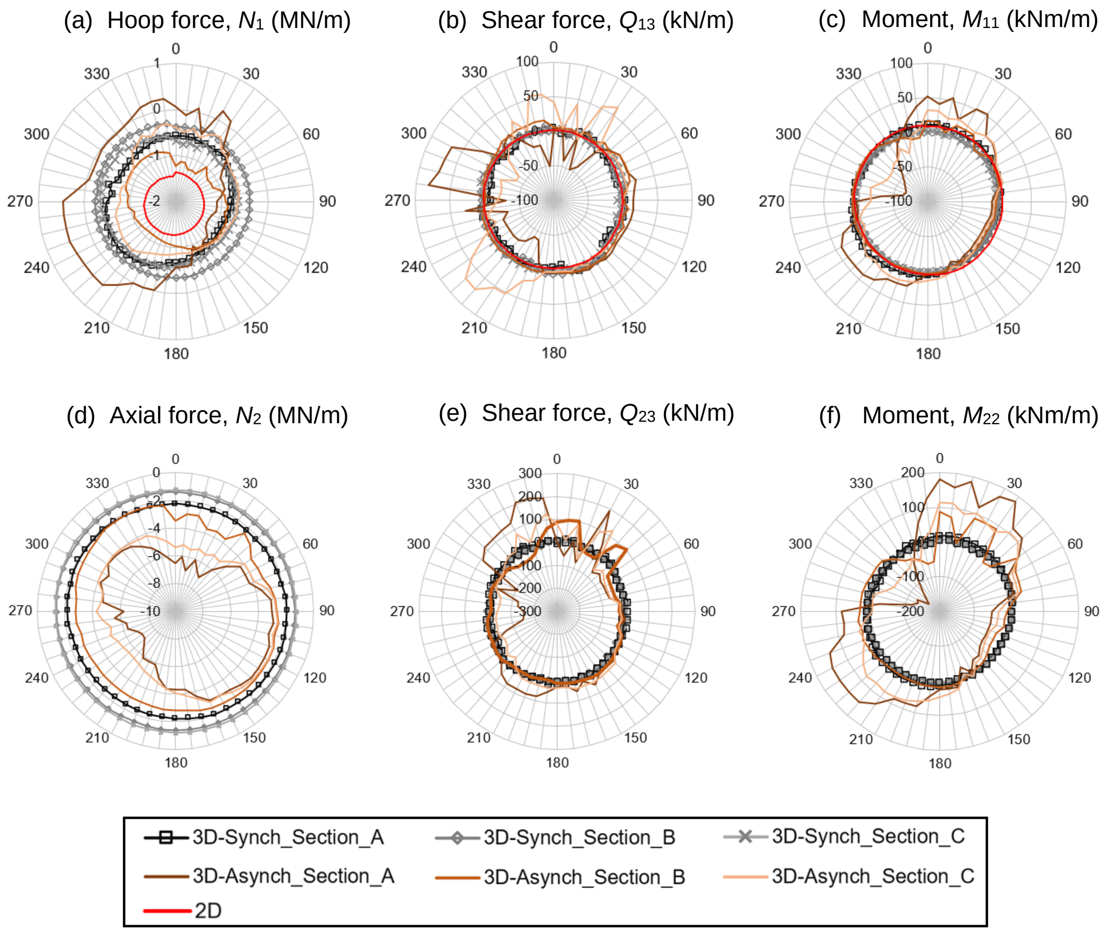

Fig 12 Peak seismic forces of the tunnel lining due to synchronous and asynchronous motion obtained at different cross-sections along the longitudinal section, where (a, b & c) are the in-plane hoop forces, and (d, e & f) are the out-of-plane forces. Note that (-*ve*) indicates compression.

The results demonstrate that while 2-D analyses may be able to reasonably capture in plane seismic bending, the effect of hoop force on the seismic bending capacity of the lining will not necessarily be well captured, even when using an advanced concrete modelling approach which inherently couples axial and bending actions, due to the absence of global scale actions (particularly axial force N_2) influencing the induced planar hoop forces (N_1).

Fig 13 shows the Axial-Moment capacity interaction diagram for a 1m lining segment at ω =10° clockwise from the tunnel centre line at sections A-C (N_1-M_{11} in plane; N_2-M_{22} out of plane). The induced actions in the asynchronous case, although larger than the synchronous actions, remained within the structural capacity of the section; however, they approached the failure surface at section-A where the largest global and local lining actions were induced. Based on the residual (post-earthquake) actions, the resilience of the tunnel along the critical length modelled would be significantly reduced for subsequent earthquakes. These residual actions are attributed primarily to plastic deformation in the surrounding ground as the tunnel lining itself remained within the elastic range for the motion considered.

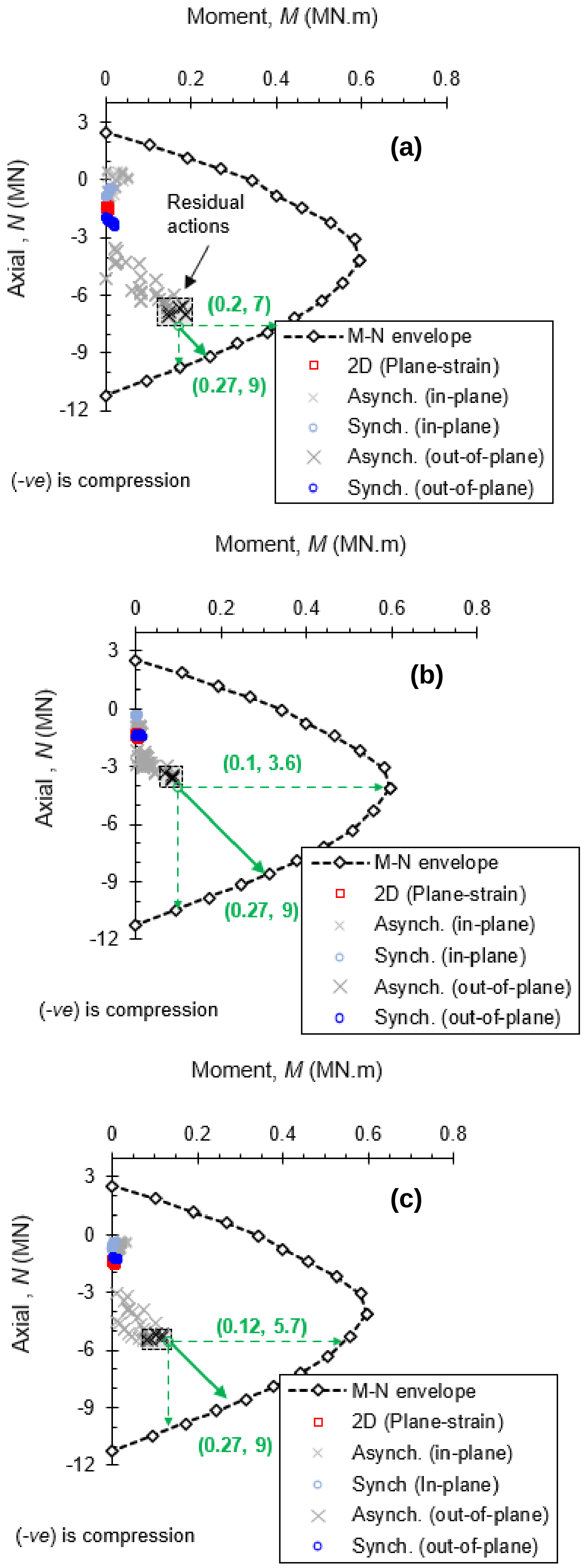

Fig 13 Axial-Moment (*N*-*M*) interaction diagrams to check the capacity of the tunnel lining at (a) section A, (b) section B and (c) section C. The green numbers indicate the coordinate values of the seismic demand point (current forces) used to evaluate the safety factor relative to the ultimate capacity envelope.

5.6 *Lining deformations*

The maximum ovalised shape at sections A, B and C along the longitudinal tunnel axis was defined at the time-step at which the resultant extension/contraction of a specific tunnel diameter $|\Delta e_{i\text{-}j}|$ was a maximum. This was determined by extracting the vertical and horizontal displacement time-histories '$u_x(t)$ & $u_y(t)$' from several closely spaced points around the circumference of the tunnel (supplementary material; Fig B5). Each diametrical line had a point at each end ($d_{i\text{-}j}$) where i was the first point and j was the corresponding second point. The resultant diametric deformation between each pair of points was calculated $|\Delta e_{i\text{-}j}(t)|$ using:

$$|\Delta e_{i\text{-}j}(t)| = \left|\sqrt{\left[u_{x,i}(t) - u_{x,j}(t)\right]^2 + \left[u_{y,i}(t) - u_{y,j}(t)\right]^2}\right| \qquad \text{Eq.2}$$

Fig 14 shows the maximum ovalised shape of the tunnel at sections A, B and C under synchronous and asynchronous boundary conditions. In all cases, the deformation had the shape of a semi-horizontal ellipse, where the deformation near the connection point at section-A was more pronounced compared to sections-B & C where the response was closer to the 2D plane-strain case. The same was true in the asynchronous case (Fig 14b), though the ovalisation was significantly larger in magnitude than for the synchronous case (note different scale of deformation). This further demonstrates the necessity of 3-D analysis over 2-D analysis for large tunnel alignments where asynchronicity may be pronounced.

Fig 15 a & b shows the time varying change in the tunnel diameter at sections A, B and C due to synchronous and asynchronous boundary conditions. For clarity, only the time-histories that correspond to the diameter with the maximum variation of $\Delta e_{i\text{-}j}$ at each section are shown. In the synchronous case (Fig 15a), the tunnel returns to the original undeformed position by the end of the earthquake (elastic response). In Fig 15b, the maximum ovalisation in the asynchronous case occurs by the end of the applied motion (along diameter $d_{4\text{-}10}$ approximately) and remains post-earthquake. In the asynchronous case, the magnitudes of the structural and ground-structure relative deformations are larger by more than one (nearly two) orders of magnitude compared to the asynchronouos case. This results in irreversible response within the surrounding ground which is 'locked-in' once the earthquake finishes. This information can be useful for assessing the post-earthquake serviceability of the tunnel, and cannot be captured by conventional 2D plane strain analyses of tunnel cross-sections.

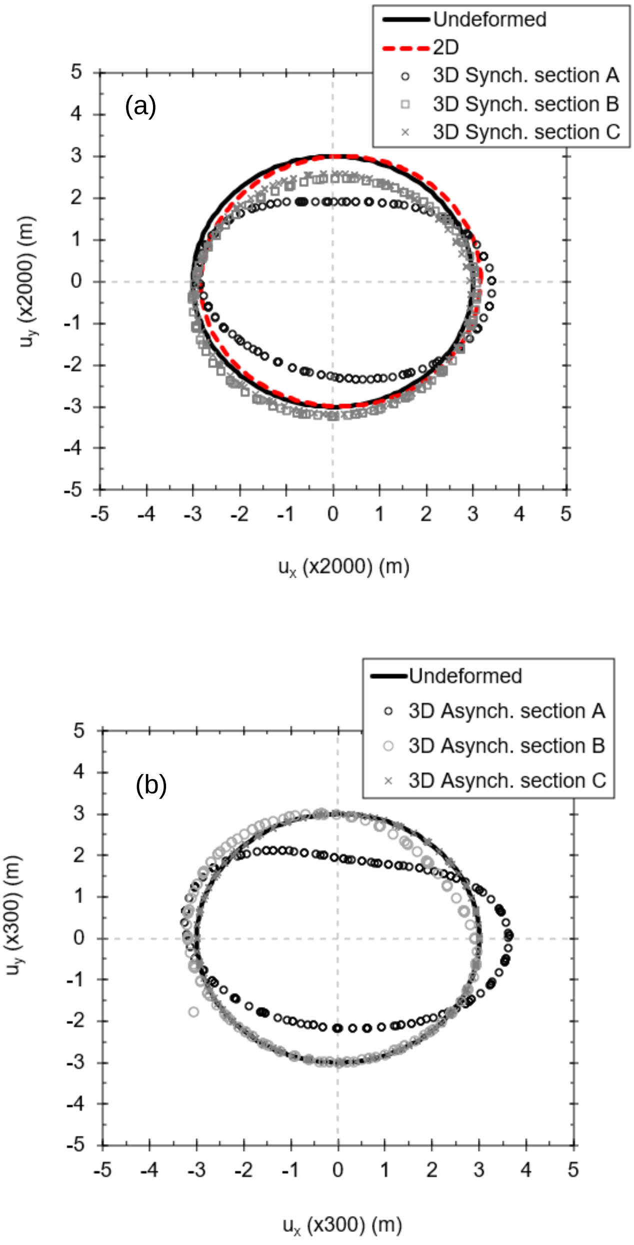

Fig 14 Seismic induced ovalisation of different sections along the longitudinal tunnel due to (a) synchronous and (b) asynchronous boundary conditions

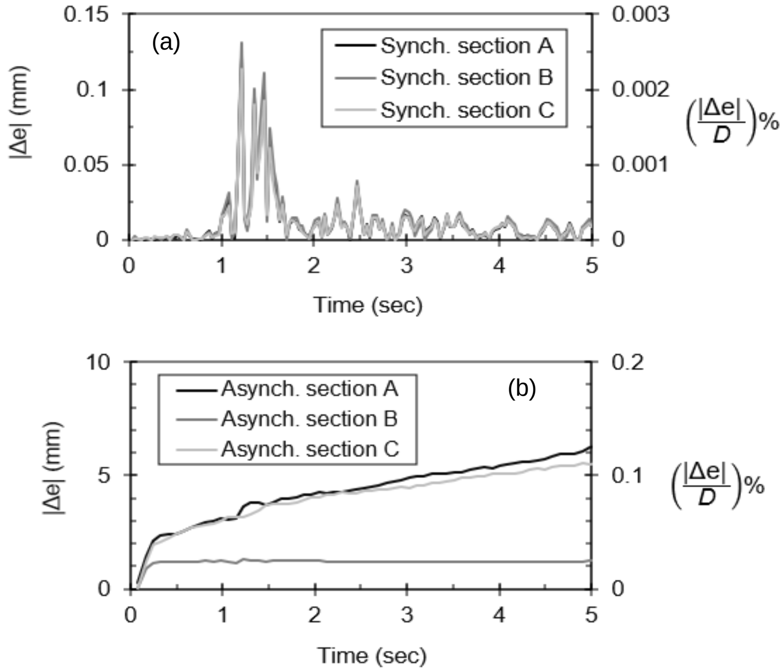

Fig 15 Variation of the tunnel diameters with time at different tunnel sections due to (a) synchronous and (b) asynchronous boundary conditions, where |Δe| is the difference in tunnel diameter and *D* is the tunnel diameter (*D* = 5200 mm).

6. Conclusions

The global seismic response of the circular, deeply-embedded LHC tunnel alignment along its full 27 km length, considering 2-D and 3-D asynchronous ground motion components, was presented in this paper. The dynamic analyses were conducted using the BNWF approach where the ground-structure interaction was modelled using parallel springs and dashpots calibrated against 2-D nonlinear FE analyses, with input motions that represent the local seismicity of the Geneva area and assuming a coherent and steady wave travelling velocity through the surrounding rock. The analyses demonstrated that long tunnel alignments can be highly susceptible to strong asynchronous ground motion effects. These are manifested as global actions (axial, moment, and shear) generated along the alignment that are not captured in conventional 2-D plane-strain analyses of particular tunnel cross-sections. Such conventional local analyses (ignoring these global effects) may therefore under-predict the lining forces and lead to under-designed sections.

The global actions are induced mainly due to differential displacement arising from either (i) differential ground-structure stiffnesses or (ii) local bending. The former appears primarily at the tunnel-cavern connection points where the transverse stiffness of the cavern is significantly larger than the transverse stiffness of the tunnel given their relative sizes. These findings would be similarly applicable to other large tunnel systems, e.g. underground mass transit systems with intermediate station boxes (‘caverns’) distributed along their length. A similar response might be anticipated for a case where a uniform alignment passes through ground with highly contrasting stiffnesses. The BNWF model can indicate the size of the region(s) that are most significantly affected, identifying critical locations for more detailed subsequent analyses. Local bending is induced due to asynchronous motion which travels wave-like through the alignment. The magnitude of the induced alignment actions is affected by the level of asynchronicity, with the effect becoming larger as the shear wave velocity of the surrounding ground reduces. Tunnel alignments that pass through softer/shallower ground may therefore see more significant effects of asynchronicity compared to those demonstrated herein for the LHC alignment.

These actions induced globally at tunnel alignment scale from the BNWF model were used as time-varying equivalent boundary multi-axial stresses on the local section of the tunnel lining, considering synchronous and asynchronous scenarios. This was demonstrated by performing a local 3-D continuum dynamic FE analysis of a critical longitudinal tunnel section (L_{crit}. = 30m) near the tunnel-cavern ‘A’ of the circular LHC tunnel alignment at CERN. The value of L_{crit} defining the size of the 3-D model was defined from the BNWF results. This second analysis stage demonstrated that:

1. Conventional 2-D plane strain dynamic FE analyses did not provide accurate representations of internal lining actions due to the influence of the global tunnel alignment geometry (including changes of stiffness at tunnel-cavern connections) and motion asynchronicity

effects at the alignment scale. Proximity to a tunnel-cavern connection and asynchronicity at the alignment scale resulted in significant increases in lining actions.

2. Axial compression induced along the tunnel at the global scale resulted in a reduction of compressive hoop stress, reducing the capacity of the reinforced concrete tunnel lining to resist co-seismically induced bending moments. Despite increased actions and reduced capacity, the LHC tunnel lining has sufficient capacity to sustain the applied design seismic actions under synchronous and asynchronous conditions at the critical location considered. However, asynchronous conditions resulted in significant residual actions at the end of the event, which would reduce resilience to future earthquakes.
3. Conventional 2-D analyses could not capture the out-of-plane tunnel lining response which appeared to exhibit higher seismic actions than the in-plane response. This demonstrates the necessity for 3-D analysis at local scale to capture this effect.
4. Ovalisation was observed in all cases. Away from the tunnel-cavern connection, the deformed shape in the 3-D case was similar to plane-strain 2-D analyses. The magnitudes of deformation were generally much larger for asynchronous loading and appeared also to be permanent, potentially affecting tunnel serviceability; the deformed shape was also significantly different in shape and magnitude at the tunnel-cavern connection.

These findings highlight that the conventional approach of decoupling transverse and longitudinal seismic analyses may not be conservative for long or curved underground structures, as alignment-scale effects can amplify local demands in ways that are not captured by isolated cross-sectional analyses.

Credit statement

Ahmad Mubarak: Methodology, Investigation, Numerical modelling, Visualisation, Writing – original draft. **Jonathan Knappett**: Conceptualization, Methodology, Writing - review & editing, Supervision, Funding acquisition. **Michael Brown**: Writing - review & editing, Supervision, Funding acquisition.

Data availability

All data created during this research are openly available from the University of Dundee Institutional Repository, Discovery at DOI: https://doi.org/10.15132/10000270

Acknowledgements

The first author is grateful for funding received from the European Organization for Nuclear Research (CERN), supporting PhD study, and for their invaluable support in providing the necessary drawings, ground investigation reports and monitoring data which were a key to achieve this work.

Declaration of competing interest

The authors declare that they have no known competing financial interests or personal relationships that could have appeared to influence the work reported in this paper.

References:

Abrahamson, N.A., Schneider, J.F. and Stepp, J.C., 1991. Empirical spatial coherency functions for application to soil-structure interaction analyses. *Earthquake spectra*, *7*(1), pp.1-27.

Amorosi, A. and Boldini, D., 2009. Numerical modelling of the transverse dynamic behaviour of circular tunnels in clayey soils. *Soil Dynamics and Earthquake Engineering*, *29*(6), pp.1059-1072.

Amorosi, A., Boldini, D. and Elia, G., 2010. Parametric study on seismic ground response by finite element modelling. *Computers and Geotechnics*, *37*(4), pp.515-528.

Anastasopoulos, I., Gerolymos, N., Drosos, V., Kourkoulis, R., Georgarakos, T. and Gazetas, G., 2007. Nonlinear response of deep immersed tunnel to strong seismic shaking. *Journal of Geotechnical and Geoenvironmental Engineering*, *133*(9), pp.1067-1090.

Bathe, K.J., 2006. *Finite element procedures*. Klaus-Jurgen Bathe.

Bentz, E.C. and Collins, M.P., 2000. Response — 2000. *Software Program for reinforced concrete sectional analysis using the modified compression field theory*, Toronto. https://response-2000.software.informer.com/1.0/

Benz, T., Vermeer, P.A. and Schwab, R., 2009. A small-strain overlay model. *International journal for numerical and analytical methods in geomechanics*, *33*(1), pp.25-44.

Bilotta, E., Maiorano, R.M.S., Viglione, A. and Aversa, S., 2015, May. Three-dimensional numerical modelling of circular tunnels under seismic actions. In *COMPDYN 20155th ECCOMAS Thematic Conference on Computational Methods in Structural Dynamics and Earthquake Engineering* (pp. 25-27). Crete Island, Greece.

BS 4449:2005. Steel for the reinforcement of concrete

Calvi, M., and Pinto, P. 1996. "Experimental and numerical investigations on the seismic response of bridges and recommendations for code provisions." *Prenormative Research in Support of Eurocode 8, Rep. 4*, European Consortium of Earthquake Shaking Tables.

CEN. 1998. EN 1998- 1:2004. Eurocode 8: Design of structures for earthquake resistance-part 1: general rules, seismic actions and rules for buildings. *Brussels: European Committee for Standardization*.

Chen, W. and Huang, G., 2010. Seismic wave passage effect on dynamic response of submerged floating tunnels. *Procedia Engineering*, *4*, pp.217-224.

Chen, Z.Y., Liang, S.B. and He, C., 2019. Influence of incoherence and wave passage effects on seismic performances of long immersed tunnel. *International Journal of Computational Methods*, *16*(05), p.1840012.

Datta, T.K. and Mashaly, E.A., 1990. Transverse response of offshore pipelines to random ground motion. *Earthquake engineering & structural dynamics*, *19*(2), pp.217-228.

Fabozzi, S., Bilotta, E., Yu, H. and Yuan, Y., 2018. Effects of the asynchronism of ground motion on the longitudinal behaviour of a circular tunnel. *Tunnelling and Underground Space Technology*, *82*, pp.529-541.

Fern, E.J., Di Murro, V., Soga, K., Li, Z., Scibile, L. and Osborne, J.A., 2018. Geotechnical characterisation of a weak sedimentary rock mass at CERN, Geneva. *Tunnelling and Underground Space Technology*, *77*, pp.249-260.

GADZ, 1996a. Reconnaissances Géologiques et Géotechniques, GADZ, 28th March 1996, doc. Ref.3545/82.

GADZ, 1996b, Geological and Geotechnical Interpretive Review, LHC Civil Engineering Consultancy Services, Package 02, Technical report, ref. S067-ST, Geneva.

GADZ, 1998*. Additional Laboratory tests*, *LHC Civil Engineering Consultancy Services, Package 02.* Technical report, ref. 11/rev. 3, Geneva.

Harichandran, R.S., Hawwari, A. and Sweidan, B.N., 1996. Response of long-span bridges to spatially varying ground motion. *Journal of Structural Engineering*, *122*(5), pp.476-484.

Haroun, M.A. and Abdel-Hafiz, E.A., 1987. Seismic response analysis of earth dams under differential ground motion. *Bulletin of the seismological society of America*, *77*(5), pp.1514-1529.

Hashash, Y.M., Hook, J.J., Schmidt, B., John, I. and Yao, C., 2001. Seismic design and analysis of underground structures. *Tunnelling and underground space technology*, *16*(4), pp.247-293.

Hashash, Y.M., Tseng, W.S. and Krimotat, A., 1998. Seismic soil-structure interaction analysis for immersed tube tunnels retrofit. *Geotechnical Special Publication*, (75 II), pp.1380-1391.

Hatzigeorgiou, G.D. and Beskos, D.E., 2010. Soil–structure interaction effects on seismic inelastic analysis of 3-D tunnels. *Soil Dynamics and Earthquake Engineering*, *30*(9), pp.851-861.

Hindy, A. and Novak, M., 1980. Pipeline response to random ground motion. *Journal of the Engineering Mechanics Division*, *106*(2), pp.339-360.

Hwang, R.N. and Lysmer, J., 1981. Response of buried structures to traveling waves. *Journal of the Geotechnical Engineering Division*, *107*(2), pp.183-200.

Kampas, G., Knappett, J.A., Brown, M.J., Anastasopoulos, I., Nikitas, N. and Fuentes, R., 2020. Implications of volume loss on the seismic response of tunnels in coarse-grained soils. *Tunnelling and Underground Space Technology*, *95*, p.103127.

Kampas, G., Knappett, J.A., Brown, M.J., Anastasopoulos, I., Nikitas, N. and Fuentes, R., 2019. The effect of tunnel lining modelling approaches on the seismic response of sprayed concrete tunnels in coarse-grained soils. *Soil Dynamics and Earthquake Engineering*, *117*, pp.122-137.

Katona, M.C. and Zienkiewicz, O.C., 1985. A unified set of single step algorithms part 3: The beta-m method, a generalization of the Newmark scheme. *International Journal for Numerical Methods in Engineering*, *21*(7), pp.1345-1359.

Kiureghian, A.D., 1996. A coherency model for spatially varying ground motions. *Earthquake engineering & structural dynamics*, *25*(1), pp.99-111.

Kontoe, S., Zdravkovic, L. and Potts, D.M., 2008. An assessment of time integration schemes for dynamic geotechnical problems. *Computers and geotechnics*, *35*(2), pp.253-264.

Kontoe, S., Zdravkovic, L., Potts, D.M. and Menkiti, C.O., 2011. On the relative merits of simple and advanced constitutive models in dynamic analysis of tunnels. *Géotechnique*, *61*(10), pp.815-829.

Kramer, S.L.,1996. *Geotechnical Earthquake Engineering*. Prentice-Hall, New Jersey, pp.100-102.

Kwok, A.O., Stewart, J.P., Hashash, Y., Matasovic, N., Pyke, R., Wang, Z. and Yang, Z., 2007. Use of exact solutions of wave propagation problems to guide implementation of nonlinear seismic ground response analysis procedures. *J. Geotech. & Geoenv. Engrg.*, *133*(11), pp.1385-1398.

Laughton, C., 1989. Construction Techniques used at Cern for the Lep Project. In *Supercollider 1* (pp. 111-124). Springer, Boston, MA.

Li, P. and Song, E.X., 2015. Three-dimensional numerical analysis for the longitudinal seismic response of tunnels under an asynchronous wave input. *Computers and Geotechnics*, *63*, pp.229-243.

Loh, C.H. and Lee, S.Z., 1990. Aseismic displacement analysis of multi-supported bridge to multiple excitations. *Soil Dynamics and Earthquake Engineering*, *9*(1), pp.25-33.

Luzi L, Puglia R, Russo E & ORFEUS WG5 (2016). Engineering Strong Motion Database. Istituto Nazionale di Geofisica e Vulcanologia, Observatories & Research Facilities for European Seismology. doi: 10.13127/ESM. See https://esm.mi.ingv.it/

Madinier, B., Canzoneri, A. and Amiot, J.B., 2017. *K3100 / Underground structures: Geotechnical Assumptions for Phase 2*. Technical Report, Geneva, Switzerland: Origin, CERN.

Mubarak, A., 2021. Python Scripts for BNWF models in ABAQUS_REV00 (DOI: 10.20933/100001310)

Mubarak, A., 2023. Numerical simulation of large tunnel systems under seismic loading conditions: CERN infrastructure as a case study, *Doctoral dissertation*, University of Dundee (UoD), UK.

Mubarak, A., Knappett, J. and Brown, M., 2023, June. Evaluation of continuum modelling approaches for reinforced concrete in geotechnical applications. In *10th European Conference on Numerical Methods in Geotechnical Engineering* (p. 216). International Society for Soil Mechanics and Geotechnical Engineering.

Mubarak, A.G., Knappett, J.A. and Brown, M.J., 2024. Influence of modelling approach for reinforced concrete underground structures, with application to the CMS cavern at CERN. *Soil Dynamics and Earthquake Engineering*, 182, p.108725.

Mubarak, A.G., Knappett, J.A. and Brown, M.J., 2025. Numerical simulation of large tunnel alignments under seismic loading: The Large Hadron Collider as a case study. *Tunnelling and Underground Space Technology*, 157, p.106315.

Mwafy, A.M., Kwon, O.S., Elnashai, A. and Hashash, Y.M., 2011. Wave passage and ground motion incoherency effects on seismic response of an extended bridge. *Journal of Bridge Engineering*, *16*(3), pp.364-374.

Novak, M. and Suen, E., 1987. Dam-foundation interaction under spatially correlated random ground motion. In *3rd Int. Conf. on Soil Dynamics and Earthquake Engineering, Elsevier, Oxford* (pp. 25-39).

Owen, G.N., Scholl, R.E., 1981. Earthquake engineering of large underground structures. Report No. FHWA/RD-80/195, Federal Highway Administration and National Science Foundation, p.279

Park, D., Sagong, M., Kwak, D.Y. and Jeong, C.G., 2009. Simulation of tunnel response under spatially varying ground motion. *Soil Dynamics and Earthquake Engineering*, *29*(11-12), pp.1417-1424.

Park, D.H., Shin, J.H. and Yun, S.U., 2010. Seismic analysis of tunnel in transverse direction part II: Evaluation of seismic tunnel response via dynamic analysis. *Journal of the Korean Geotechnical Society*, *26*(6), pp.71-85.

Pitilakis, K. and Tsinidis, G., 2014. Performance and seismic design of underground structures. In *Earthquake geotechnical engineering design* (pp. 279-340). Cham: Springer International Publishing.

PLAXIS 3D, (2021) Plaxis 3D, Reference Manual, pp 1–611. https://communities.bentley.com/products/geotech-analysis/w/plaxissoilvision-wiki/46137/manuals---plaxis

Power, M. S., Rosidi, D., and Kaneshiro, J. 1996. "Vol. III: Screening, evaluation, and retrofit design of tunnels." *Research Rep.*, National Center for Earthquake Engineering Research, State Univ. of New York, Buffalo.

Roy, N. and Sarkar, R., 2017. A review of seismic damage of mountain tunnels and probable failure mechanisms. *Geotechnical and Geological Engineering*, *35*(1), pp.1-28.

Schweiger, H. F., Marcher, T., & Schädlich, B. (2014). Application of a novel constitutive shotcrete model to tunneling. In *Rock Engineering and Rock Mechanics: Structures in and on Rock Masses: EUROCK 2014*; CRC Press Taylor & Francis Group: Leiden, The Netherlands; pp. 799–804.

Sextos, A., Kappos, A., and Pitilakis, K. 2003a. "Inelastic dynamic analysis of RC bridges accounting for spatial variability of ground motion, site effects, and soil-structure interaction phenomena. Part 2: Parametric study." *Earthquake Eng. Struct. Dyn.*, 32, 629–652.

Sextos, A., Pitilakis, K., and Kappos, A. 2003b. "Inelastic dynamic analysis of RC bridges accounting for spatial variability of ground motion, site effects, and soil-structure interaction phenomena. Part 1: Methodology and analytical tools." *Earthquake Eng. Struct. Dyn.*, 32, 607–627

Vanmarcke, E.H., Heredia-Zavoni, E. and Fenton, G.A., 1993. Conditional simulation of spatially correlated earthquake ground motion. *Journal of Engineering Mechanics*, *119*(11), pp.2333-2352.

Wilson, J.C. and Jennings, P.C., 1985. Spatial variation of ground motion determined from accelerograms recorded on a highway bridge. *Bulletin of the Seismological Society of America*, *75*(6), pp.1515-1533.

Yan, X., Yuan, J., Yu, H., Bobet, A. and Yuan, Y., 2016. Multi-point shaking table test design for long tunnels under non-uniform seismic loading. *Tunnelling and Underground Space Technology*, *59*, pp.114-126.

Yang, Y., Wang, X., Zhou, Z., Zhang, X. and Li, Z. 2023. Seismic analysis of underground tunnels subjected to 3D oblique incident P and SV waves by 2.5D approach. Underground Space, 12, pp.271-286.

Yashiro, K., Kojima, Y. and Shimizu, M., 2007. Historical earthquake damage to tunnels in Japan and case studies of railway tunnels in the 2004 Niigataken-Chuetsu earthquake. *Quarterly Report of RTRI*, *48*(3), pp.136-141.

Yu, H., Yang, Y. and Yuan, Y., 2018a. Analytical solution for a finite Euler–Bernoulli beam with single discontinuity in section under arbitrary dynamic loads. *Applied Mathematical Modelling*, *60*, pp.571-580.

Yu, H., Yuan, Y., Qiao, Z., Gu, Y., Yang, Z. and Li, X., 2013. Seismic analysis of a long tunnel based on multi-scale method. *Engineering structures*, 49, pp. 572-587.

Yu, H., Yuan, Y., Xu, G., Su, Q., Yan, X. and Li, C., 2018b. Multi-point shaking table test for long tunnels subjected to non-uniform seismic loadings-part II: Application to the HZM immersed tunnel. *Soil Dynamics and Earthquake Engineering*, *108*, pp.187-195.

Yuan, Y., Yu, H., Li, C., Yan, X. and Yuan, J., 2018. Multi-point shaking table test for long tunnels subjected to non-uniform seismic loadings–Part I: Theory and validation. *Soil Dynamics and Earthquake Engineering*, *108*, pp.177-186.

Zerva, A., 1990. Response of multi-span beams to spatially incoherent seismic ground motions. *Earthquake Engineering & Structural Dynamics*, *19*(6), pp.819-832.

Zhang, L. and Chopra, A.K., 1991. *Computation of spatially varying ground motion and foundation-rock impedance matrices for seismic analysis of arch dams* (Vol. 91, No. 6). Earthquake Engineering Research Center, University of California.

Zhang, S., Yuan, Y., Li, C., Chen, H. and Chen, Z., 2021. Seismic responses of long segmental immersed tunnel under unfavorable loads combination. *Transportation Geotechnics*, *30*, p.100621.

Zienkiewicz, O.C., Bicanic, N. and Shen, F.Q., 1989. Earthquake input definition and the transmitting boundary conditions. In *Advances in computational nonlinear mechanics* (pp. 109-138). Springer, Vienna.

Figure captions:

Figure 1: (a) Overview of the existing LHC underground complex © CERN, and (b) simplified plane-view of the circular LHC tunnel alignment adopted for the ground-strucutre interaction model.

Figure 2: (a) Simplified sketch for the BNWF model of the circular LHC tunnel alignment and (b) vertical shafts; H_R (*t*): are the resultant dynamic displacement component in the radial and circumferential directions.

Figure 3: Assignment of the asynchronous amplitude vectors to the spring's boundaries assuming Eastwards seismic wave propagation

Figure 4: (a) 3D FE model of the longitudinal section at the critical region near the tunnel-cavern-A connection, and (b) FE model of the modelled 3D longitudinal tunnel section showing the location of key tunnel cross sections for result extraction.

Figure 5: (a) Normalised Axial-Normalised Moment (*N*-*M*) interaction diagram, and (b) Normalised Moment-Curvature (*M*-*κ*) of the LHC tunnel section

Figure 6: (a) Schematic view of the location of the modelled longitudinal tunnel segment and (b) the different action components in the 'in-plane' and 'out-of-plane' directions that were obtained from the BNWF model of the circular LHC tunnel at the critical region near Cavern-A.

Figure 7: Peak seismic force envelopes due to 3-D Synchronous and Asynchronous Eastwards wave propagation, where (a), (d) & (g) are forces distribution along the circular alignment; (b), (e) & (h) show forces at the tunnel-cavern-A connection; (c), (f) & (i) are time histories obtained at the connections to caverns 'A' &'B' respectively.

Figure 8: Directionality effect of propagated seismic wave on the peak seismic force envelopes along the circular alignment, where (a), (b) & (c) are forces distribution due to North-eastwards

propagation; (d), (e) & (f) are forces distribution due to Northwards propagation, both compared with the Eastwards propagation.

Figure 9: Fourier amplitude spectrum for dominant component of the local Swiss motion ($a_{\mathrm{H1}}(t)$ with PGA = 0.15g)

Figure 10: Effect of shear wave velocity (or wave travel time) on the tunnel alignment forces considering 2D and 3D wave combinations.

Figure 11: Sign convention for the obtained lining forces in the transverse (x-axis) and the longitudinal/axial (y-axis) directions. Note that (-*ve*) is compression.

Figure 12: Peak seismic forces of the tunnel lining due to synchronous and asynchronous motion obtained at different cross-sections along the longitudinal section, where (a, b & c) are the in-plane hoop forces, and (d, e & f) are the out-of-plane forces. Note that (-*ve*) indicates compression.

Figure 13: Axial-Moment (N-M) interaction diagrams to check the capacity of the tunnel lining at (a) section A, (b) section B and (c) section C.

Figure 14: Seismic induced ovalisation of different sections along the longitudinal tunnel due to (a) synchronous and (b) asynchronous boundary conditions

Figure 15 Variation of the tunnel diameters with time at different tunnel sections due to (a) synchronous and (b) asynchronous boundary conditions, where "$|\Delta e|$" is the difference in tunnel diameter and D is the tunnel diameter (D = 5200 mm)

Notations list

Symbol	Unit	Description
LHC		Large Hadron Collider
CMS		Compact Muon Solenoid
ATLAS		A Toroidal LHC ApparatuS
BNWF		Beam-on-Nonlinear-Winkler Foundation
FEA		Finite Element Analysis
RC		Reinforced Concrete
ESM		Engineering Strong Motion
BGL	[m]	Below Ground Level
PGA	[g or m/s^2]	Peak ground acceleration, where g = 9.81 m/s^2
P	[GN]	Load
δ	[mm]	Displacement
G_0	[MPa]	Initial shear stiffness at small strains
$\gamma_{0.7}$	[-]	Shear strain when the secant shear stiffness G degrades to 70% of the initial shear stiffness, G_0
$D\%$	[-]	Damping ratio`
p^{ref}	[kPa]	Reference atmospheric pressure = 100 kPa
γ_{sat}	[kN/m^3]	Saturated soil/rock unit weight
V_a	[m/s]	Apparent shear wave velocity
V_s	[m/s]	Shear wave velocity
X_i	[m]	Wave travel distance
θ	[°]	In-plane angle between the tunnel alignment and the direction of the travelling wave
$L_{crit.}$	[m]	Critical tunnel length
l_s	[m]	Spacing between Winkler springs
l_e	-	Mesh element characteristic length
c'	[MPa]	Cohesive strength
φ'	[°]	Friction angle
ψ	[°]	Dilatancy angle
ϕ_{max}	[°]	Maximum friction angle
E_{28}	[MPa]	28 days Young's modulus
E_{ur}	[MPa]	Unloading-reloading stiffness
$E_{oed.}$	[MPa]	Oedometer 'tangent' stiffness
E_{50}	[MPa]	Secant stiffness 'drained triaxial'
E_s	[MPa]	Modulus of elasticity of steel
m	[-]	Power for stress-level dependency of stiffness
v	[-]	Poisson's ratio
$f_{c,28}$	[MPa]	Uniaxial compressive strength
$f_{t,28}$	[MPa]	Uniaxial tensile strength
$f_{c0,n}$	[-]	Normalised initially mobilised strength
$f_{cf,n}$	[-]	Normalised failure strength
$f_{cu,n}$	[-]	Normalised residual strength

ε_{cp}^{p}	[-]	Uniaxial plastic failure strain
$G_{c,28}$	[kN/m]	Compressive fracture energy
$G_{t,28}$	[kN/m]	Tensile fracture energy
$f_{tu,n}$	[-]	Ratio of residual vs. peak tensile strength
f_y	[MPa]	Tensile yield strength of steel
EI	[GN.m^2]	Flexural stiffness
EA	[GN/m]	Axial stiffness
N_p	[kN/m]	Tensile yield strength
r	[m]	Tunnel radius
D	[m]	Tunnel diameter
z	[m]	Tunnel running depth
κ	[rad/km]	Curvature
c	[GN.s/m]	Dashpot coefficient
t_0	[seconds]	Wave arrival time
t-lag	[seconds]	Total wave lag time
$u_x(t)$ and $u_y(t)$	[m]	Horizontal and vertical tunnel displacement vector, respectively
a_g	[m/s^2]	Ground acceleration
M_w	-	Earthquake Moment Magnitude
$a_{H1}(t)$	[m/s^2]	Dominant (in-plane) horizontal acceleration component
$a_{H1}(t)$	[m/s^2]	Secondary (in-plane) horizontal acceleration component
$a_v(t)$	[m/s^2]	Vertical (out-of-plane) acceleration component
$H_1(t)$	[m]	Dominant displacement amplitude vector
$H_2(t)$	[m]	Secondary displacement amplitude vector
$H_R(t)$	[m]	Resultant displacement amplitude vector
λ	[m]	Seismic wave length
f	[Hz]	Seismic wave frequency
f_m and f_n	[Hz]	Target frequency(ies)
D^*	%	Target damping
C_1 and C_2	-	Normal and tangential relaxation coefficients, respectively.
α_N and β_N	-	Time integration parameters
M_z	[MN.m]	In-plane bending in the tunnel alignment
V_x	[MN]	In-plane shear in the tunnel alignment
N_y	[MN]	In-plane axial force in the tunnel alignment
A_{hoop}	[m^2]	Tunnel hoop area
A_s	[mm^2]	Area of steel
N_1	[MN]	In-plane hoop axial force
Q_{13}	[MN]	In-plane hoop shear force
M_{11}	[MN.m]	In-plane hoop moment force
N_2	[MN]	Out-of-plane hoop axial force
Q_{23}	[MN]	Out-of-plane hoop shear force
M_{22}	[MN.m]	Out-of-plane hoop moment force
T	[MN.m]	Torque
$\lvert\Delta e_{i\text{-}j}(t)\rvert$	[m]	Resultant time-varying change in tunnel diameter
σ_n	[kN/m^2]	Axial stress

σ_n	[kN/m^2]	Shear stress
σ'_{ci}	[MPa]	Unconfined compressive strength of intact rock
σ_z	[MPa]	Vertical total stress

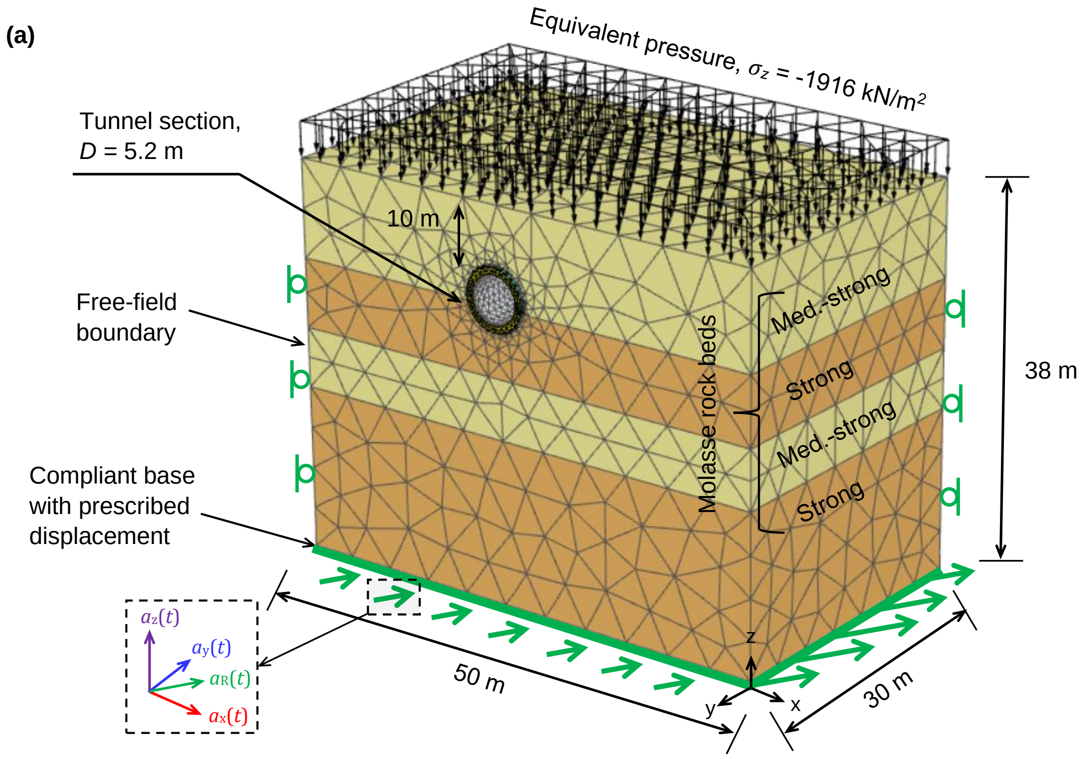
(a)
Equivalent pressure, σ_z = -1916 kN/m^2
Tunnel section, D = 5.2 m
10 m
Free-field boundary
Compliant base with prescribed displacement
Molasse rock beds
Med.-strong
Strong
Med.-strong
Strong
38 m
50 m
30 m
z
y
x
$a_z(t)$
$a_y(t)$
$a_R(t)$
$a_x(t)$

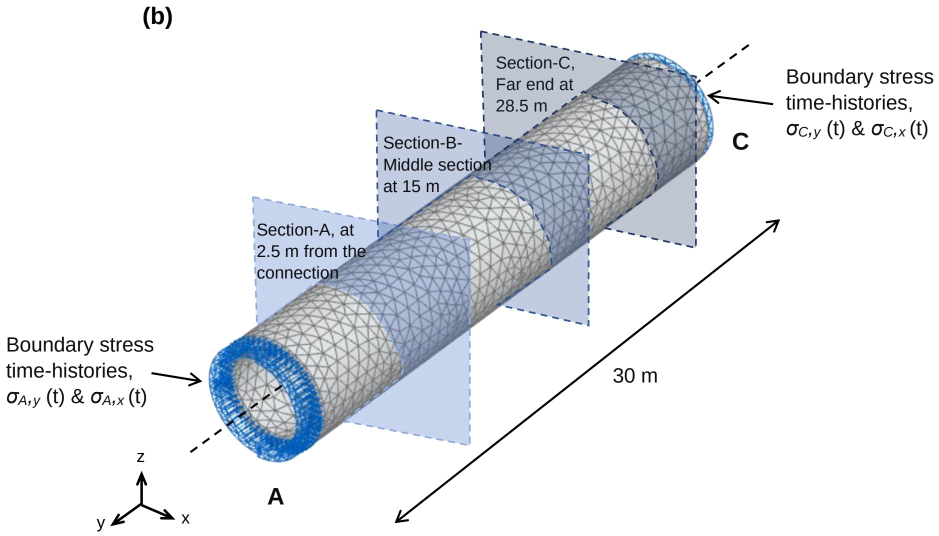

Fig 4 (a) 3D FE model domain of the longitudinal section at the critical region near the tunnel-cavern-A connection, and (b) FE model of the modelled 3D longitudinal tunnel lining only, showing the location of key tunnel cross sections for result extraction.

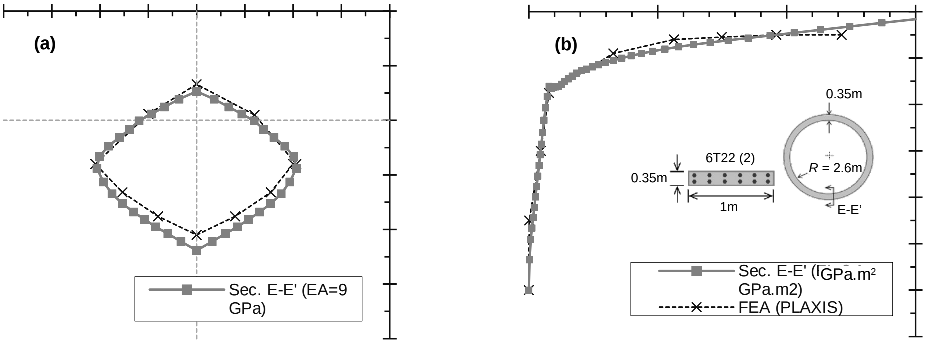

Fig 5 (a) Normalised Axial-Normalised Moment (*N*-*M*) interaction diagram, and (b) Normalised Moment-Curvature (*M*-*κ*) of the LHC tunnel section

σ_n	[kN/m^2]	Shear stress
σ'_{ci}	[MPa]	Unconfined compressive strength of intact rock
σ_z	[MPa]	Vertical total stress

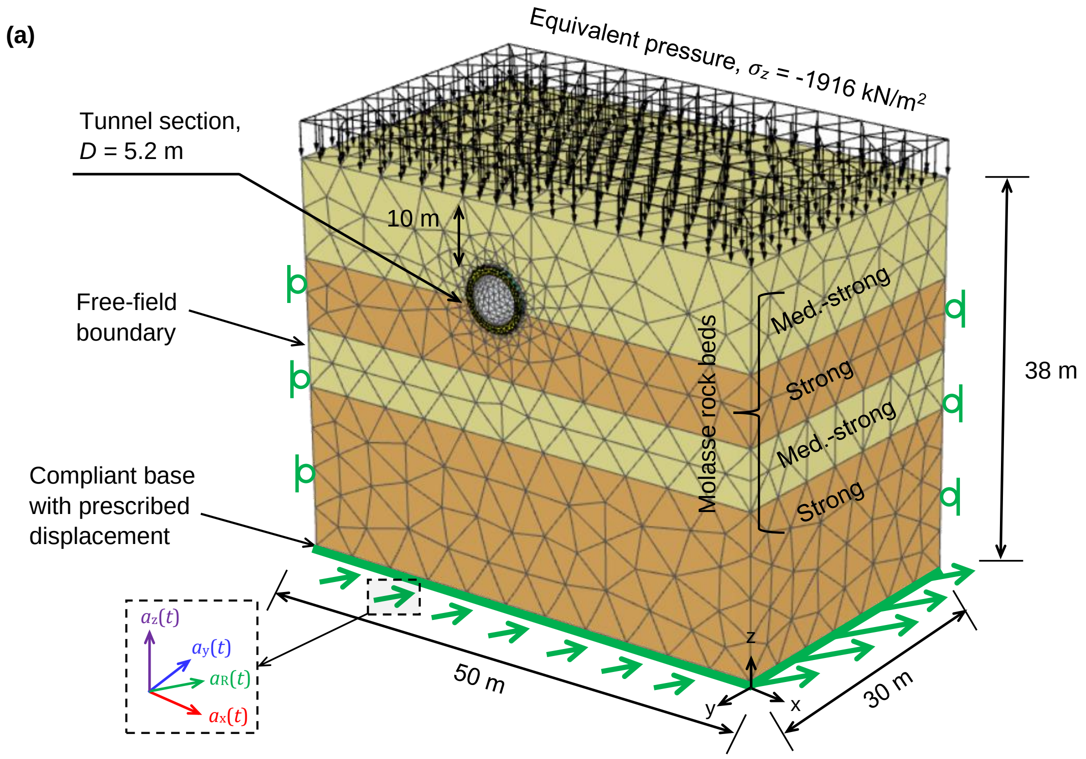
(a)
Equivalent pressure, σ_z = -1916 kN/m^2
Tunnel section,
D = 5.2 m
10 m
Free-field
boundary
Compliant base
with prescribed
displacement
Molasse rock beds
Med.-strong
Strong
Med.-strong
Strong
38 m
50 m
30 m
z
y
x
$a_z(t)$
$a_y(t)$
$a_R(t)$
$a_x(t)$

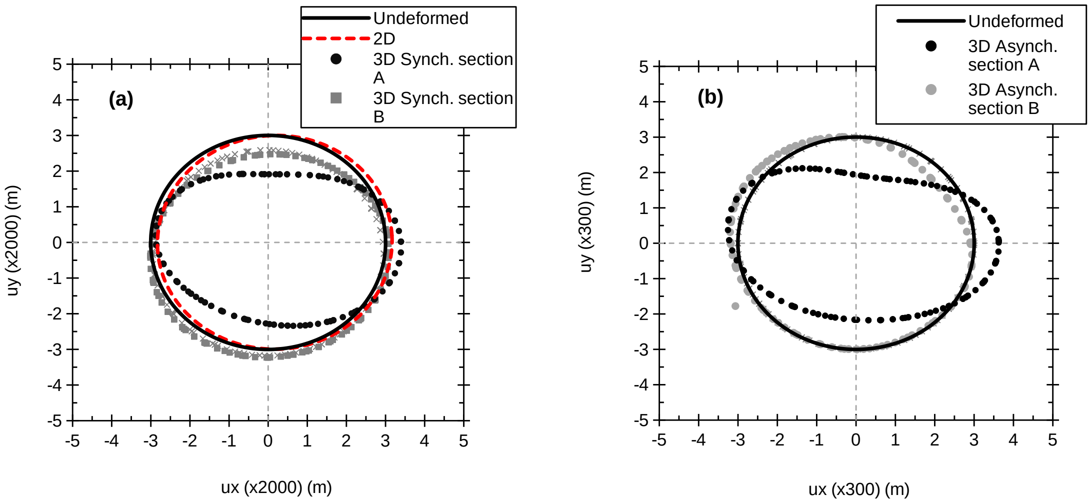

Fig 14 Seismic induced ovalisation of different sections along the longitudinal tunnel due to (a) synchronous and (b) asynchronous boundary conditions

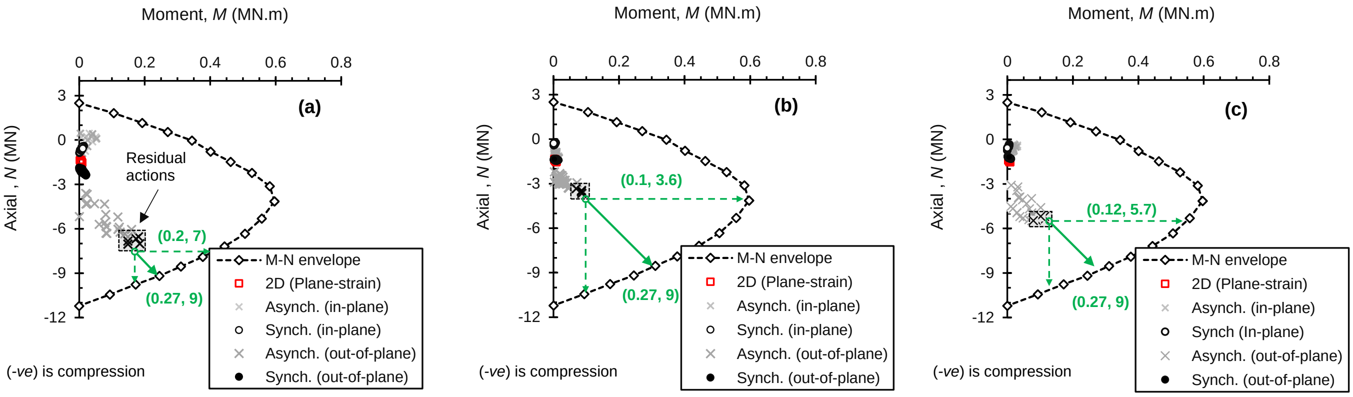
Moment, *M* (MN.m)
0
0.2
0.4
0.6
0.8
3
0
-3
-6
-9
-12
Axial , *N* (MN)
(a)
Residual actions
(0.2, 7)
(0.27, 9)
(-*ve*) is compression
M-N envelope
2D (Plane-strain)
Asynch. (in-plane)
Synch. (in-plane)
Asynch. (out-of-plane)
Synch. (out-of-plane)
(b)
(0.1, 3.6)
(0.27, 9)
(c)
(0.12, 5.7)
(0.27, 9)
Synch (In-plane)

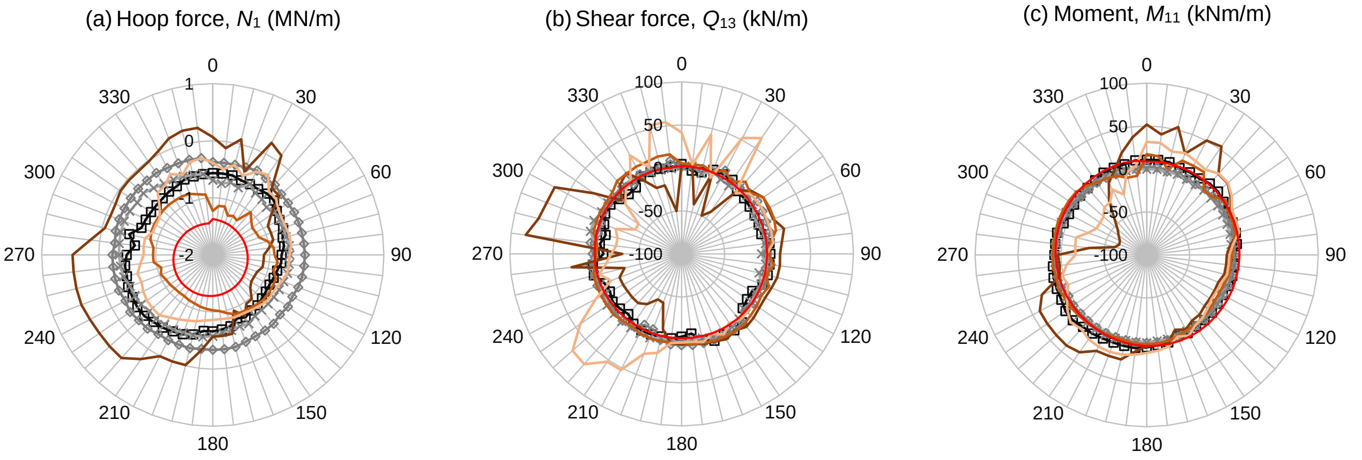
(a) Hoop force, N_1 (MN/m)
(b) Shear force, Q_{13} (kN/m)
(c) Moment, M_{11} (kNm/m)
0
30
60
90
120
150
180
210
240
270
300
330
1
0
-1
-2
100
50
0
-50
-100

1

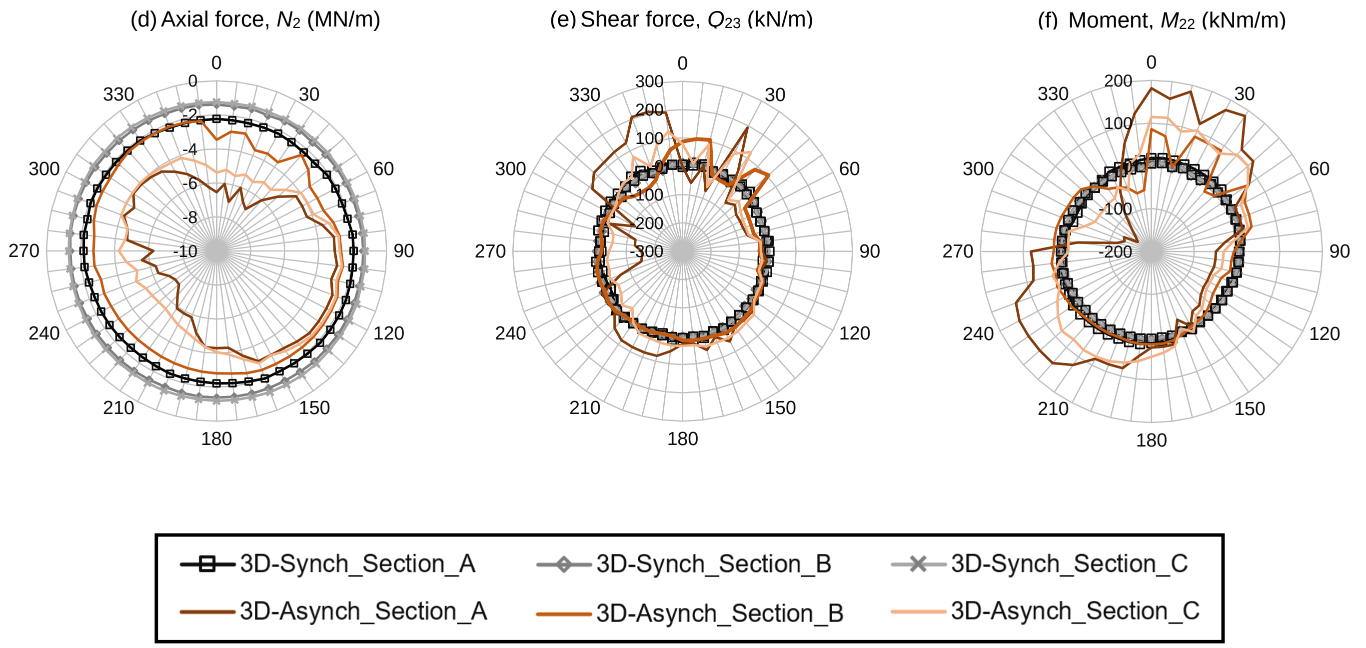
(d) Axial force, N_2 (MN/m)
(e) Shear force, Q_{23} (kN/m)
(f) Moment, M_{22} (kNm/m)
0
30
60
90
120
150
180
210
240
270
300
330
0
-2
-4
-6
-8
-10
300
200
100
0
-100
-200
-300
200
100
0
-100
-200
3D-Synch_Section_A
3D-Synch_Section_B
3D-Synch_Section_C
3D-Asynch_Section_A
3D-Asynch_Section_B
3D-Asynch_Section_C

2

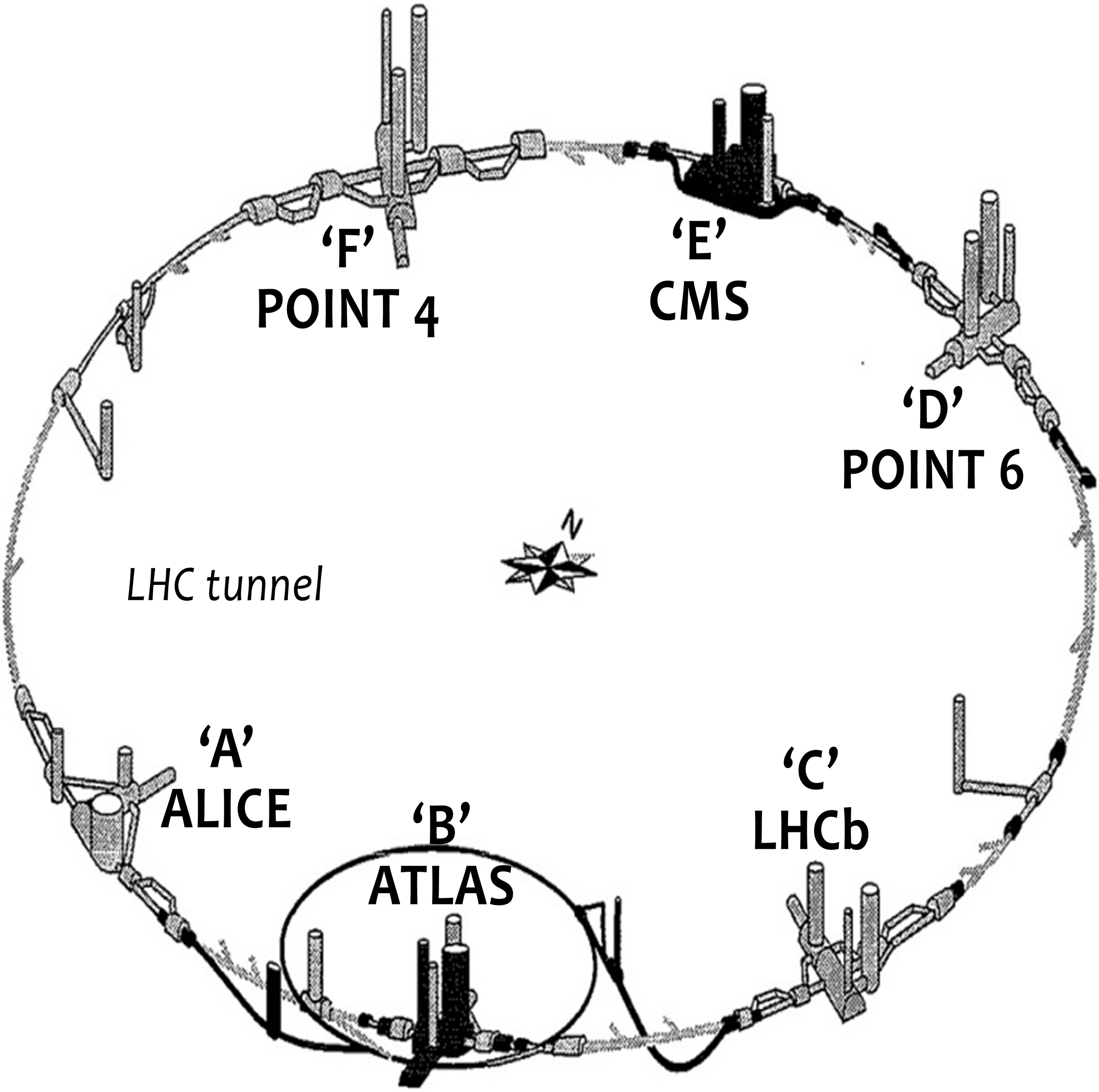
‘F’
POINT 4
‘E’
CMS
‘D’
POINT 6
N
LHC tunnel
‘A’
ALICE
‘B’
ATLAS
‘C’
LHCb

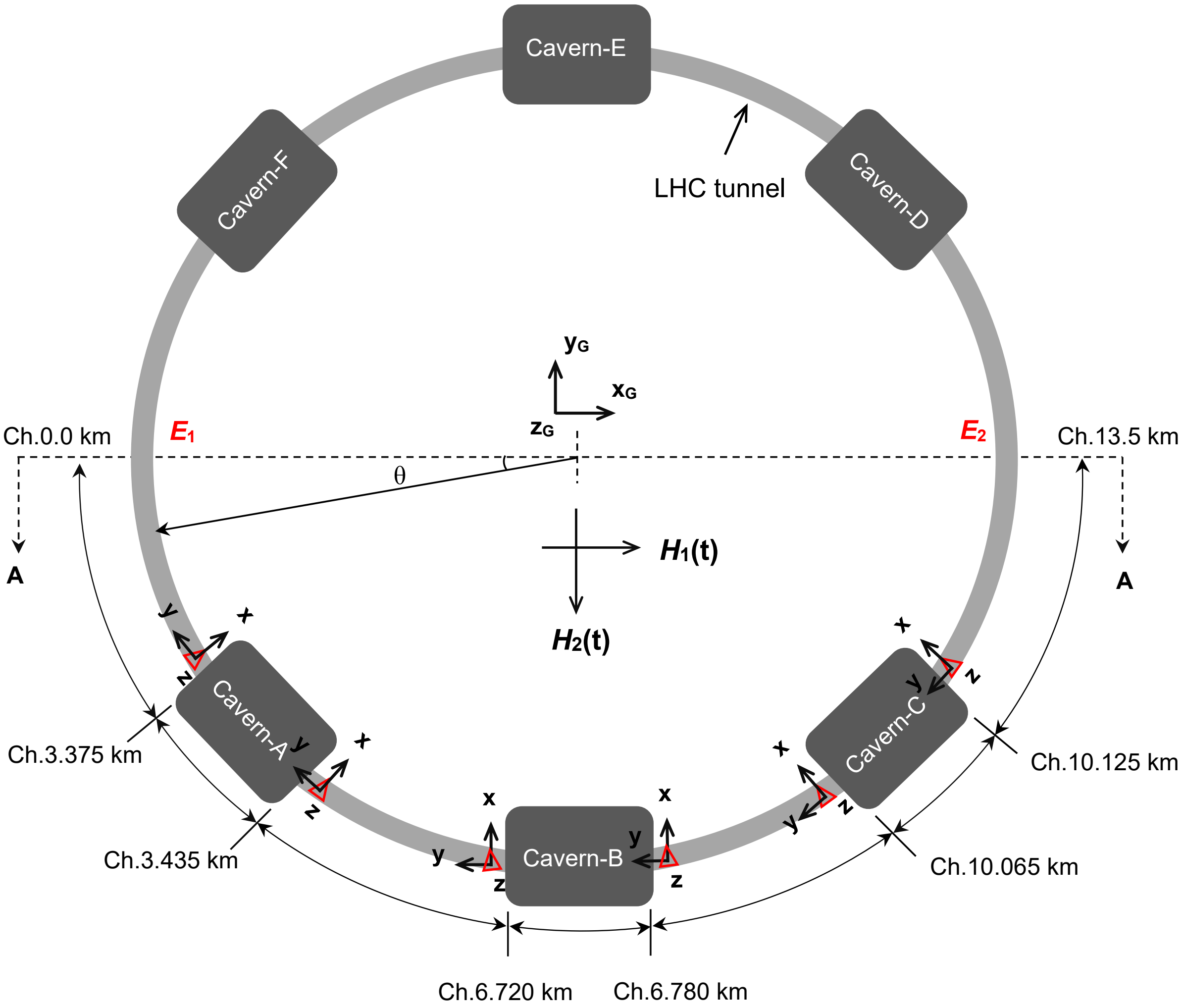

Figure 1: (b) simplified plane-view of the circular LHC tunnel alignment adopted for the ground-strucutre interaction model.

(a)

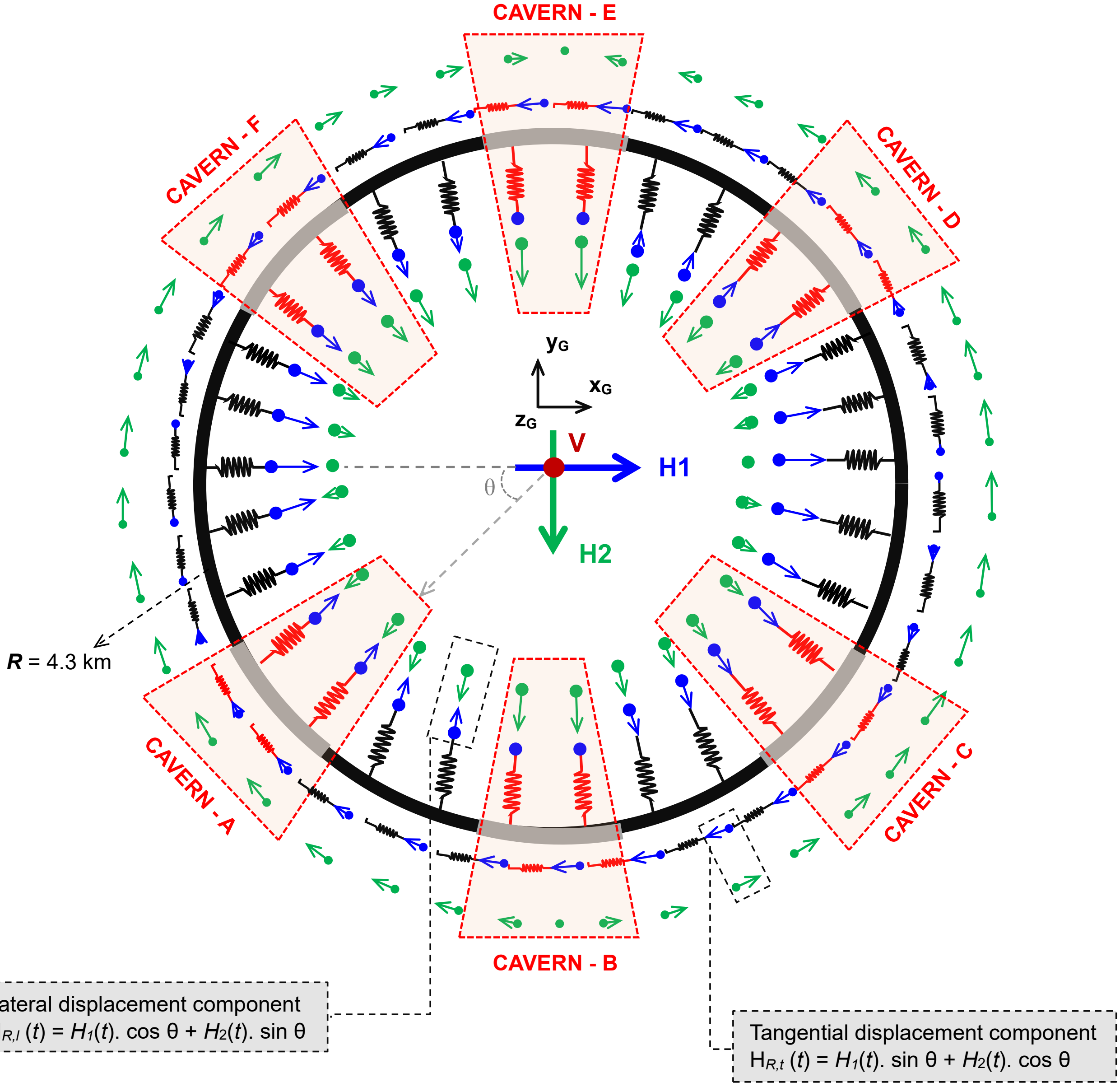

Lateral displacement component
$H_{R,l}\,(t) = H_1(t).\cos\theta + H_2(t).\sin\theta$

Tangential displacement component
$H_{R,t}\,(t) = H_1(t).\sin\theta + H_2(t).\cos\theta$

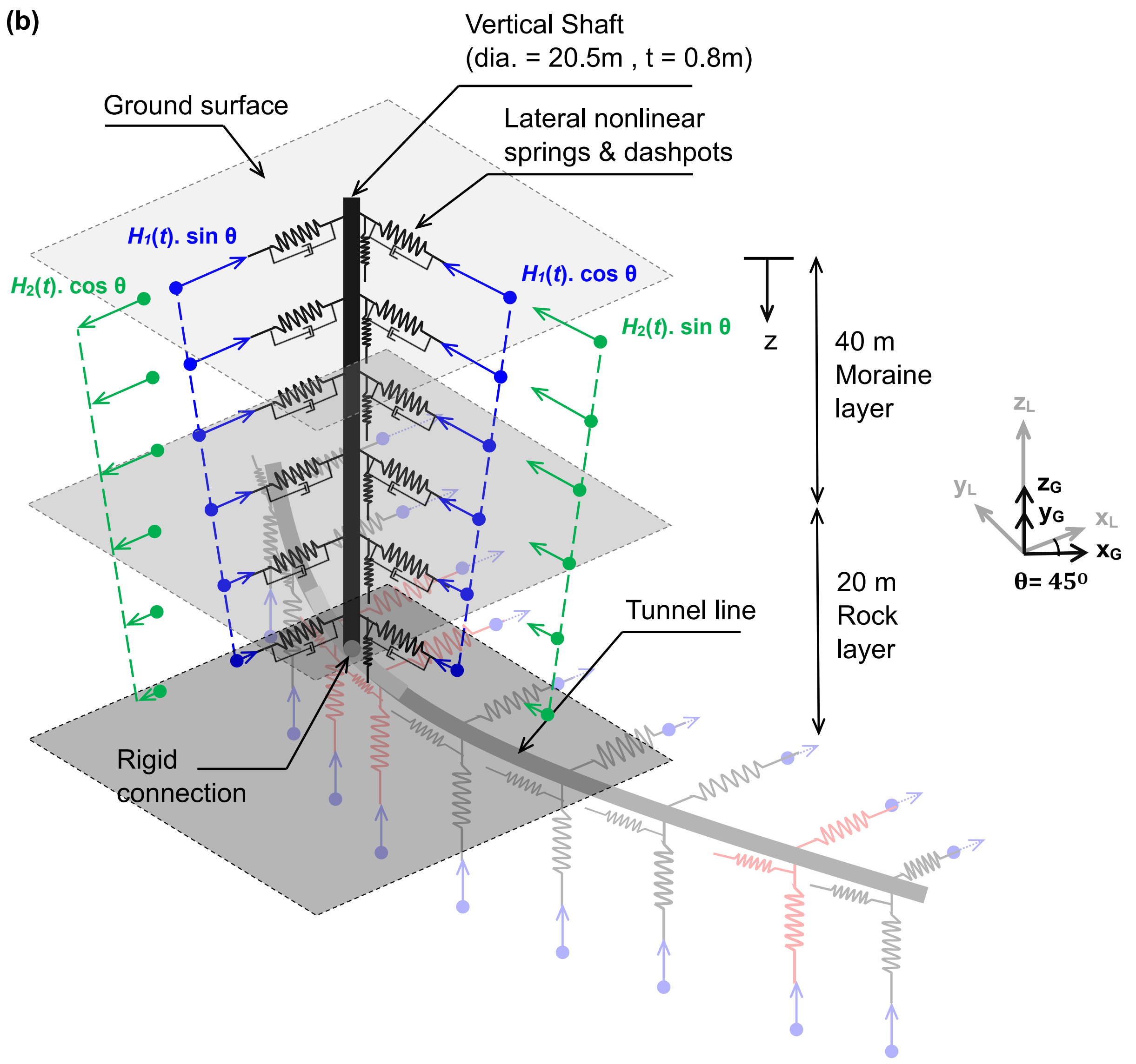

Figure 2 (a) Simplified sketch for the BNWF model of the circular LHC tunnel alignment and (b) vertical shafts; $H_R\,(t)$: are the resultant dynamic displacement component in the lateral and tangential directions

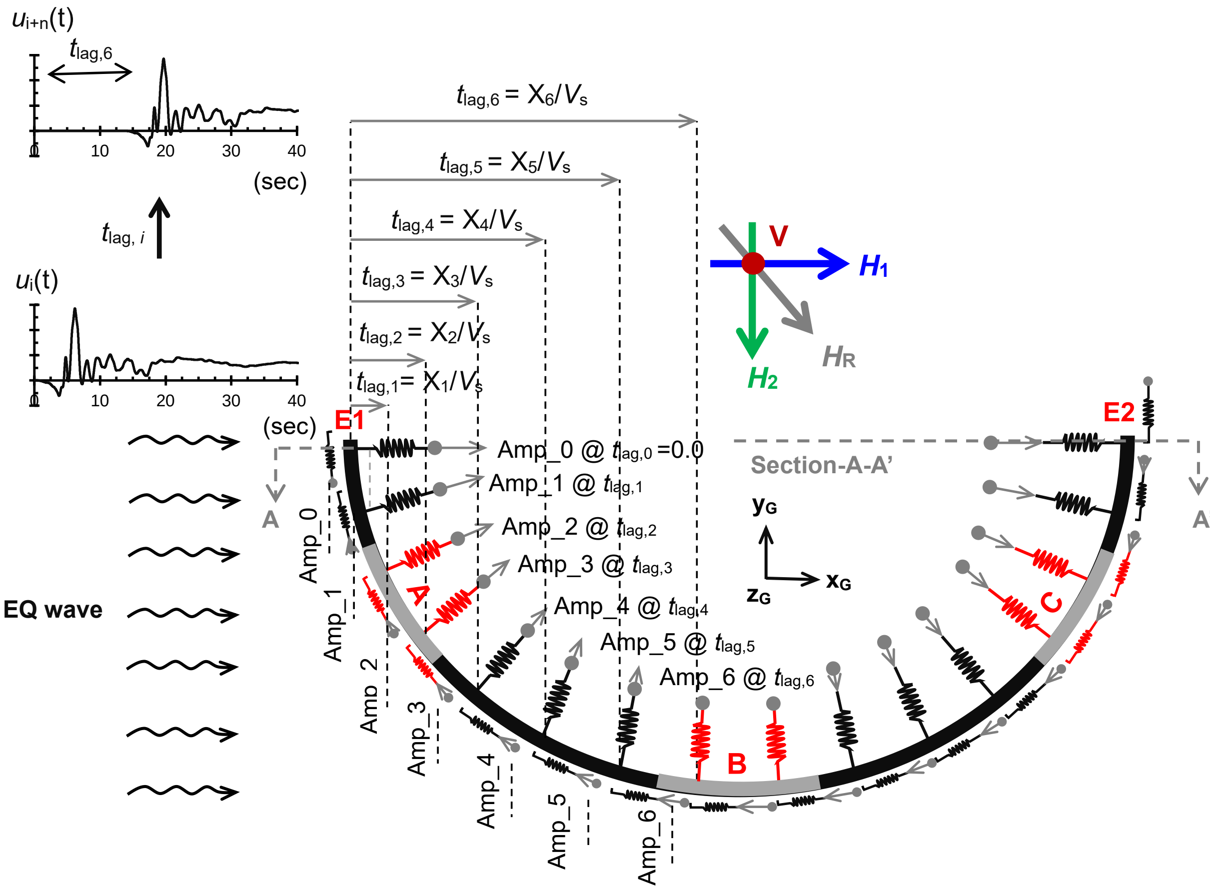

Figure 3 Assignment of the asynchronous amplitude vectors to the spring's boundaries